THESIS FOR THE DEGREE OF DOCTOR OF PHILOSOPHY

Plasmonics with a Twist: from Single Particles to Metasurfaces

ROBIN OGIER

CHALMERS

Department of Physics
CHALMERS UNIVERSITY OF TECHNOLOGY
Göteborg, Sweden 2016

Plasmonics with a Twist: from Single Particles to Metasurfaces
Robin Ogier

ISBN 978-91-7597-337-1

Doktorsavhandlingar vid Chalmers tekniska högskola
Ny serie nr. 4018
ISSN 0346-718X

Department of Applied Physics
Chalmers University of Technology
SE-412 96 Göteborg
Sweden
Telephone +46 (0)31 772 1000

Cover picture

1: *Illustration of a right-handed tetramer*

2: *Illustration of a metasurface composed elongated nanoparticles.*

3: *Rotating nanorod under the action of circularly polarized light.*

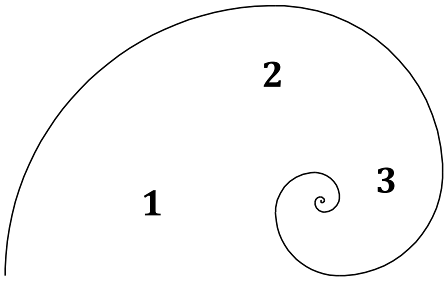

Printed by Chalmers Reproservice
Göteborg, Sweden 2016

Plasmonics with a Twist: from Single Particles to Metasurfaces
Robin Ogier
Department of Physics
Chalmers University of Technology

Abstract

Nanophotonics deals with how electromagnetic fields can be confined and squeezed to orders of dimensions below the light wavelength. Plasmonics, one of the fields of nanophotonics, study collective free electron oscillations driven by light in metallic nanostructures and interfaces. The greater part of plasmonics applications utilizes the plasmons light localization property and the resulting enhanced photon density of states. Plasmonic effects can also be used to harvest and modify photon angular momentum. In this thesis, plasmonics is used in two different ways: 1) to induce rotation in optically trapped gold nanoparticles, and 2) to create chiroptically active metasurfaces.

Optical tweezers was pioneered in the early 1970s by the work of A. Ashkin. As its name suggests, optical tweezers allow for precise control of the position and movement of small objects with light. This can be used for manipulation of fragile samples, such as living cells, and nanoparticles with nanometer-level precision, as well as for sensing of forces in the piconewton range. Adding rotation frequency control to the set of features applicable to a trapped particle could expand the utility of optical tweezers to nanoscale viscosity probing, mixing in micro- and nanofluidics, and microtooling of soft matter. In this thesis, gold nanoparticles, trapped by a 2D optical trapping setup against an interface, were set in rotation using a circularly polarized laser beam. The absorbed and scattered photons possess an intrinsic spin angular momentum that generate an optical torque, which is balanced by a drag force from the surrounding water. The power dependence of the rotation frequencies could be well fitted by classic electromagnetism and hydrodynamic theories. Additionally, the light induced heating of the nanoparticles at higher laser powers was shown to strongly influence the friction of the enclosing liquid. New measurements on nanorods rotating against a water-oil interface showed increased rotation frequencies, possibly due to a particle orientation change. Rotating nanoparticles could offer a new route to probe interfaces as well as being nanoscale sources of emulsion.

In order to manipulate photon angular momentum, nanoparticle metasurfaces were fabricated with a focus on breaking their overall geometrical symmetry. The main technique used was hole-mask colloidal lithography, which is low cost, high speed, and offers large area coverage. Based on this method, and thanks to metallic angular and rotating evaporation techniques, diverse nanostructure patterns with increased feature control were developed. Starting from a simple geometrical principle, chirality, two types of metasurfaces were investigated. Both showed pronounced optical activity, that is, different optical response to illumination with right- or left-handed circularly polarized light. In the case of tetramers built from particles with different height, forming a staircase, an intrinsic chiral response was induced through strong near-field coupling and phase retardation effects. In the case of anisotropic particle layers, an evanescent illumination configuration resulted in extrinsic chirality, which allowed for a contrast of around 90% in reflection between right- and left-handed circularly polarized light. This effect arises from the illumination geometry, the polarization-dependent excitation efficiency of the nanoparticles with respect to their orientation, and the density of dipoles on the surface. The observed phenomena might be utilized in, for example, polarization manipulation and enantiomer sensing.

Taken together, the results presented in this thesis offer some new insights into the fascinating interaction between circularly polarized light and plasmonics nanoparticles. The results may also provide as well a platform for further development of complex nanostructures for basic studies and diverse plasmonic applications.

Keywords: localized surface plasmons, metasurfaces, optical trapping, nanofabrication, colloidal lithography, chirality, circularly polarized light

List of appended papers

This thesis is based on the work presented in the following publications:

I. **Ultrafast Spinning of Gold Nanoparticles in Water Using Circularly Polarized Light**
Lehmuskero, A. ; Ogier, R. ; Gschneidtner, T. ; Johansson, P. ; Käll, M.
Nano Letters, **2013**, *13(7)*, pp 3129-3134

II. **Macroscopic Layers of Chiral Plasmonic Nanoparticle Oligomers from Colloidal Lithography**
Ogier, R. ; Fang, Y. ; Svedendahl, M. ; Johansson, P. ; Käll, M.
ACS Photonics, **2014**, *1(10)*, pp 1074-1081

III. **Near-Complete Photon Spin Selectivity in a Metasurface of Anisotropic Plasmonic Antennas**
Ogier, R. ; Fang, Y. ; Käll, M. ; Svedendahl, M.
Physical Review X, **2015**, *5(4)*, 041019

IV. **Continuous Gradient Plasmonic Nanostructures Fabricated by Evaporation on a Partially Exposed Rotating Substrate**
Ogier, R. ; Shao, L. ; Svedendahl, M. ; Käll, M.
Submitted Manuscript

My contribution to the appended papers

I. I participated in the optical measurements and resulting discussions, and drafted parts of the paper.

II. I fabricated the samples and took part in the optical experiments, performed parts of the numerical simulations, participated in the data analysis and resulting discussions and drafted the paper.

III. I fabricated the samples and took part in the optical experiments. I participated in the discussions of the data and drafted parts of the paper.

IV. I fabricated parts of the samples and participated in the optical measurements. I took part in the data analysis and resulting discussions and wrote the first draft of the paper.

Publications not included in this thesis

The following publications are outside the scope of this thesis:

V. **Dimer-on-Mirror SERS Substrates with Attogram Sensitivity Fabricated by Colloidal Lithography**
Hakonen, A. ; Svedendahl, M. ; Ogier, R. ; Yang, Z.-J. ; Lodewijks, K. ; Verre, R. ; Shegai, T. ; Andersson, P. O. ; Käll, M.
Nanoscale, **2015**, *7*, pp 9405-9410

VI. **Plasmon Enhanced Internal Photoemission in Antenna-Spacer-Mirror Based Au/TiO2 Nanostructures**
Fang, Y. ; Jiao, Y. ; Xiong, K. ; Ogier, R. ; Yang, Z.-J. ; Gao, S. ; Dahlin, A. B. ; Käll, M.
Nano Letters, **2015**, *15(6)*, pp. 4059-4065

Contents

Chapter 1

Introduction

Light is one of the most important conveniences in our everyday life. It allows us to perceive objects, volumes, and materials. What we call visible light is proper to our species. The colours we perceive, which is based on the photoreceptors located in our retina, interpret the world around us in a particular way. For example, unlike humans who have three different colour sensitive cells in their retina (red, green, and blue), dogs have only two (blue and yellow). The mantis shrimp has one of the most elaborate visual systems ever discovered and their eyes carry 16 types of colour receptive cones. We couldn't understand a world seen through their eyes. Light lets living beings probe the properties of matter. For instance, we will suppose that a reflective object is made from metal and insects will go to plants whose colours have evolved in an attractive form to them.

An aspect of light often forgotten is its polarization. The ability to manipulate the polarization of light is essential to numerous applications including spectroscopy, microscopy, telecommunications, etc. One of the earliest applications of a material whose properties depend on the light polarization is the use of Iceland spar by navigators to tell the direction of the sun in cloudy and twilight conditions. Since then control of linearly polarized light has progressed by leaps and bounds and is as common as going to the cinema to watch a 3D movie.

Circular polarization is another important type of light polarization. In the case of linearly polarized light, the light wave oscillates in a plane as it travels forward. For circularly polarized light, imagine that the light wave is a corkscrew moving forward. Of course, any corkscrew found in a kitchen rotates to the right. For light, one has both right-handed and left-handed circularly polarized light. Probed with circularly polarized light, certain objects behave differently depending on the light handedness. Among them, some are at the origin of life itself such as DNA and the amino-acids. They all possess a geometrical property called chirality. Chirality was defined by Lord W. T. Kelvin in 1904 as the following:[1]

"I call any geometrical figure, or group of points, chiral, and say it has chirality if its image in a plane mirror, ideally realized, cannot be brought to coincide with itself."

Chirality of molecules became very important during the advent of stereochemistry, started in 1874 by A. Le Bel and J. H. van't Hoff.[2, 3] Getting information about the handedness of molecules is important in the development of effective drugs. The main way, to this day, of quantifying molecular chirality is by measuring the so-called circular dichroism. However, molecules interact very weakly with light and chirality signals are therefore low.

On the other hand, metallic nanoparticles interact very strongly with light. The most famous historically example of the use of colloidal metal particles are the Lycurgus cup, a Roman chalice from the 4th century, and the colourful stained glass windows in medieval European cathedrals. It is only in the 19th century that the optical properties of gold particles were investigated in a scientific manner by M. Faraday.[4] Then, G. Mie continued the research and proposed a theory to predict the optical properties of spherical particles.[5] According to Mie theory, the colour of a metallic sphere depends on the sphere dimensions, on the dielectric function of the material composing the sphere, and on the dielectric function of the surrounding medium. Nowadays, the electromagnetic waves coupled resonantly to the free electron plasma of a conducting nanoparticle, and at the origin of its colour, are called localized surface plasmons (LSPs).

Advances in nanofabrication techniques paved the way to the development of chiral plasmonic nanostructures. Contrary to the weak interaction of chiral molecules which is due to the mismatch in size between the molecule scale and the circularly polarized light helical pitch, plasmonic nanoparticles are within the correct size range to obtain strong optical chirality, as has been reported for artificial metamaterials in multiple articles.[6-8] As chiral structure geometries developed, their potential for applications expanded to include, for example, broadband polarizers, enantioselective sensing platforms, negative refractive index metamaterials and optical communication devices.[9-12]

On a closely related subject, light has the ability to interact mechanically with matter. This was first observed by J. Kepler in 1619 when following the direction of a comet's tail with respect to its position to the sun.[13] Later, in 1986, A. Ashkin and coworkers created the optical tweezers.[14] Optical tweezers techniques have since been used for over 30 years to manipulate and study the properties of micro- and nanometer-sized particles. The ability to achieve displacements with nanometer accuracy and measure forces down to the piconewton level has opened up new areas of study in biology, chemistry, and physics, such as the observation of single molecules, DNA properties and single metallic nanoparticles.[15-17] Circularly polarized light has also its importance here. Indeed, each circularly polarized photon carries a spin angular momentum able to induce an optical torque on matter. Rotating nanoparticles are of interest for micro-rheology sensing, microfluidics actuators, and propellers.

Supporting the progresses in nanotechnology, nanofabrication advances are critical in defining what are the next nanostructures available. Top-down techniques, such as photolithography and electron-beam lithography, are widely used in research. Hole-mask colloidal lithography is a quicker and cheaper method. It can produce homogeneous nanostructured layers over large areas. However it has its limitations, such as accuracy and features design. Pushing the limits of fabrication methods by the integration of new variables, such as tilted evaporation or surface chemistry, may diversify plasmonic applications.

This thesis focuses on the interaction of circularly polarized light with plasmonic nanoparticles and plasmonic metasurfaces. Chapter 2 introduces the basics of surface plasmons based on different simple models. One can start by considering a single nanoparticle as a dipolar antenna coupled to an external electromagnetic field. But as the number of particles increases, interaction mechanisms need to be included to account for the effect of each dipole on its neighbours. Increasing the number of particles to densily fill a whole layer results in a metasurface, a new category of material with properties sometimes not found in nature. In Chapter 3 shows how plasmonic particles can mimic a geometrical property of crucial importance in nature: chirality. This symmetry-breaking approach is a convenient way to couple to circularly polarized light. Different strategies are available, such as the realization of spirals, tetrahedrons, or the simpler extrinsic chirality. Chapter 4 is dedicated to optical trapping. By means of circularly polarized light, optical torque can be applied on nanoparticles, which can be set in rotation at frequencies of several tens of kilohertz. Included in that chapter, observations on the rotation of nanorods at an oil-water interface are presented. Nanofabrication has been a large part of my PhD worth. Its evolution can be seen through Papers II, III, and IV. Chapter 5 completes what can be read from my papers by adding some process details. A summary and outlook of my overall work is given in Chapter 6.

Chapter 2

Surface Plasmons

The work presented in this thesis deals with plasmonic nanoparticles either on a substrate or in solution. Depending on the number of nanostructures, one can employ a great variety of models. Single nanoparticles can be viewed as dipolar optical nanoantennas,[18-21] few neighbouring nanoparticles interact and couple together to hybridize similarly to molecular bonds,[22, 23] and an array of nanoparticles can be thought of as a metasurface with macroscopic optical properties.[24, 25] This indicates how complex the optical properties of nanostructures can be. Thus, if we want to understand the optical characteristics of such systems, some basic physical considerations are needed. Here, I will try to provide some basic insights into plasmonic systems.

Plasmonics describes the electromagnetic response of metals over a wide wavelength range. It can be explained classically by solving Maxwell's equations.[26] The optical properties of free electron metals follow the plasma model. When an electromagnetic field is applied, the free electrons in the metal oscillate collectively against the fixed positive ions. These oscillations are the so-called plasmons. However, this approach is limited at visible frequencies for noble metals, such as gold and silver, due to their interband transitions from bound electrons and the associated strong absorption. On the other hand, for alkali metals the range can be extended to the ultraviolet. When the impinging electromagnetic field excites a propagating plasmon at the interface between a conductor and a dielectric, one has surface plasmon polaritons (SPPs).[27, 28] If instead of a continuous interface, one has a finite conducting nanoparticle of any shape, the electromagnetic waves couple to non-propagating plasmons, also called localized surface plasmons (LSPs).[5]

In general, plasmons can be excited in any kind of metallic sample. Nonetheless, certain conditions must be met for SPPs to be excited on planar metallic surfaces. To generate LSPs in a metallic nanoparticle, direct light illumination is sufficient, and the LSPs detection is straightforward. In this chapter, surface plasmons are described for a variety of systems. First, a short presentation is made on the modelling of noble metals optical properties. Then, I go over the equations leading to a description of SPPs in a semi-infinite system. Third, spheroid metallic nanoparticles are considered, and the conditions to achieve dipole surface plasmons are discussed. Fourth paragraph is about the coupled dipole approximation model to simply calculate interactions between nanoparticles. The fifth part is a brief introduction to the modified Fresnel coefficients, used in the case of a nanoparticle metasurface.

2. 1 The Drude model

When we look at metals in our daily life, they appear highly reflective for frequencies up to the visible and do not allow external electromagnetic fields to penetrate through them. As a consequence they are usually used as waveguides for microwave and far-infrared technologies where the perfect conductor approximation is valid. Towards the near-infrared and visible range of the spectrum, the electromagnetic field penetrates deeper, which therefore leads to higher dissipation.

At optical frequencies, the properties of metals are described by a complex dielectric constant, ε. The dielectric function of a metal can thus be written as a function of the frequency, ω, as $\varepsilon(\omega) = \varepsilon_r(\omega) + i\,\varepsilon_I(\omega)$. In the free electron approximation, applying an electromagnetic field induces an oscillation from the electrons damped through collisions. These collisions occur at a characteristic average collision frequency, $\gamma = 1/\tau$. The electrons are associated to an effective mass m and an elementary charge e. One can summarize this via the following equation of motion:[29]

$$m\frac{d^2\boldsymbol{x}}{dt^2}+m\gamma\frac{d\boldsymbol{x}}{dt}=-e\boldsymbol{E} \tag{2. 1}$$

, where $\boldsymbol{x}$ is the position of the electron with respect to the core centre. If we assume $\boldsymbol{E}$ to be an harmonic oscillation, it can be rewritten as $\boldsymbol{E}(t) = \boldsymbol{E}_0 exp(-i\omega t)$. Thus, equation (2. 1) has a particular solution of the form $\boldsymbol{x}(\omega, t) = \boldsymbol{x}_0(\omega) exp(-i\omega t)$, and upon substitution one can find:

$$\boldsymbol{x}(t)=\frac{e}{m(\omega^2+i\gamma\omega)}\boldsymbol{E}(t) \tag{2. 2}$$

When the electrons are displaced, each electron creates a dipole moment $\boldsymbol{p} = -e\boldsymbol{x}_0$ that adds up to an induced macroscopic polarization $\boldsymbol{P} = N\boldsymbol{p}$, where N is the number of electrons per unit volume. Then, the polarization can be written as:

$$\boldsymbol{P}=\frac{-Ne^2\boldsymbol{E}_0}{m(\omega^2+i\gamma\omega)} \tag{2. 3}$$

The polarization is related to the dielectric constant and the permittivity of free space, ε_0, via according to literature:[29]

$$\boldsymbol{P}=\epsilon_0(\epsilon-1)\boldsymbol{E}_0 \tag{2. 4}$$

Substituting equation (2. 4) into (2. 3) allows us to reach the expression for the complex dielectric function, $\varepsilon(\omega)$:

$$\epsilon(\omega)=1-\frac{\omega_p^2}{\omega^2+i\gamma\omega} \tag{2. 5}$$

, where $\omega_p^2 = Ne^2/\varepsilon_0 m$ is the so-called plasma frequency of the free electrons.[30, 31] Equation (2. 5) is also known as the Drude model.[32] The real and imaginary parts of the dielectric function can be further expressed as:

$$\begin{aligned}\epsilon_r(\omega)&=1-\frac{\omega_p^2}{\omega^2+\gamma^2}\\ \epsilon_I(\omega)&=\frac{\omega_p^2\gamma}{\omega(\omega^2+\gamma^2)}\end{aligned} \tag{2. 6}$$

If we are only working at frequencies $\omega < \omega_p$, the metal keeps its metallic behaviour. Frequencies near ω_p are large, leading to $\gamma << \omega$. Under this assumption, $\varepsilon(\omega)$ becomes:

$$\epsilon(\omega)=1-\frac{\omega_p^2}{\omega^2} \tag{2. 7}$$

Although equation (2. 7) is the result of many assumptions and simplifications, it remains useful in the understanding of metal optical properties. The corresponding complex refractive index, $n(\omega)$ with $\varepsilon(\omega) = n(\omega)^2$, is mainly imaginary, meaning that the reflection coefficient is close to 1, and the electromagnetic field decreases exponentially inside the metal. However, in the case of real metals, such as silver and gold, interband transitions occurring at near-infrared and visible wavelengths modify the dielectric function. Interband transitions can be described by the equation of motion:

$$m\frac{d^2\boldsymbol{x}}{dt^2}+m\gamma\frac{d\boldsymbol{x}}{dt}+m\omega_0^2\boldsymbol{x}=-e\boldsymbol{E} \tag{2. 8}$$

, which represents electrons bound to the atom experiencing a restoring force and with a resonance frequency, ω_0. Using equation (2. 8) together with equation (2. 5) and recalculating the polarization adds Lorentzian terms to the free electrons solution to account for the interband transitions.

After getting a clearer view of the optical characteristics of metals, one can approach a system composed of an interface composed of a dielectric and a conductor and how SPPs are formed.

2. 2 Surface plasmon polaritons

SPPs-based biosensors have become a staple tool for the investigation of biomolecular binding and general refractometric sensing. When excited, a SPP will give rise to a drop in intensity of the reflected light. A change in the refractive index of the dielectric medium alters the coupling condition between the light wave and the SPP. This can be observed as a change in the properties of the light wave such as coupling

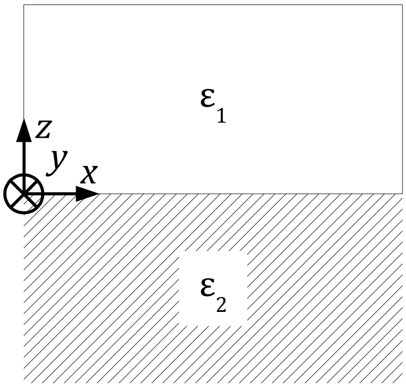

Figure 2.1: Schematic used for the derivation of the surface plasmons conditions. Two semi-infinite media are separated by an interface at *z = 0*.

wavelength, intensity, and phase for example. Nowadays, a SPPs-based sensor can measure changes in the refractive index down to 10^{-7} RIU.[33]

In order to investigate the physical properties of SPPs, we now consider the case of two semi-infinite nonmagnetic media with respective dielectric functions ε_1 and ε_2. Their interface is located at *z = 0*, such as depicted in Figure 2.1. This classical problem is solved by starting from the Maxwell's equations in the absence of external sources. Maxwell's equations are given by:[26]

$$\begin{gathered}\nabla\times\boldsymbol{H}_i=\epsilon_i\frac{1}{c}\frac{\partial}{\partial t}\boldsymbol{E}_i\\ \nabla\times\boldsymbol{E}_i=-\frac{1}{c}\frac{\partial}{\partial t}\boldsymbol{H}_i\\ \nabla\cdot(\epsilon_i\boldsymbol{E}_i)=0\\ \nabla\cdot\boldsymbol{H}_i=0\end{gathered}\tag{2. 9}$$

, where the index *i = 1, 2* depends on the *z* position. By solving this set of equations, it can usually be shown that two groups of solutions are possible. They correspond to the *s*-polarized (or TE) and *p*-polarized (or TM) modes, also equivalent to the electric field ***E*** and magnetic field ***H*** being parallel to the interface, respectively. Assuming the surface is ideal, propagating waves occur along the surface if the component of the electric field normal to the interface is non-zero. Thus, *s*-polarized surface plasmon polaritons can not exist and we are left with finding the conditions for which a TM-wave can propagate along the propagation direction *x* at the interface *z = 0* and with evanescent decay perpendicular to it. The electric and magnetic wave fields can be expressed as:

$$\begin{gathered}\boldsymbol{E}_i=(E_{ix},0,E_{iz})\exp(-\varsigma_i z)\exp(i(k_i x-\omega t))\\ \boldsymbol{H}_i=(0,E_{iy},0)\exp(-\varsigma_i z)\exp(i(k_i x-\omega t))\end{gathered}\tag{2. 10}$$

, where k_i is the wave-vector parallel to the surface, and ς_i is a positive constant such that the waves are bound to the interface.

Using equations (2. 10) in equations (2. 9) reduces the system of equations to:

$$\begin{aligned} i\varsigma_1 H_{1y} &= +\frac{\omega}{c}\epsilon_1 E_{1x} \\ i\varsigma_2 H_{2y} &= -\frac{\omega}{c}\epsilon_2 E_{2x} \end{aligned} \tag{2. 11}$$

, and

$$\varsigma_i = \sqrt{k_i^2 - \epsilon_i \frac{\omega^2}{c^2}} \tag{2. 12}$$

Due to boundary conditions, the electric and magnetic fields components parallel to the surface must be continuous. Applying the continuity condition to equations (2. 11) and (2. 12) leads to:

$$\begin{aligned} \frac{\varsigma_1}{\epsilon_1} H_{1y} + \frac{\varsigma_2}{\epsilon_2} H_{2y} &= 0 \\ H_{1y} - H_{2y} &= 0 \end{aligned} \tag{2. 13}$$

Solving the equations set (2. 13) results in:

$$\frac{\epsilon_1}{\varsigma_1} + \frac{\epsilon_2}{\varsigma_2} = 0 \tag{2. 14}$$

, which is the surface plasmons condition.

Moreover, if the media on the two sides of the interface have their dielectric constants with opposite signs, SPPs can exist only under the condition that $\varsigma_i > 0$. By substituting equation (2. 12) in equation (2. 14), it follows that $k_1 = k_2 = k$ and we arrive at the following equation:[34]

$$k = \frac{\omega}{c}\sqrt{\frac{\epsilon_1 \epsilon_2}{\epsilon_1 + \epsilon_2}} \tag{2. 15}$$

This result is the dispersion relation of SPPs propagating at the interface between two semi-infinite media. For a metal-dielectric interface, choosing vacuum characterized by $\varepsilon_2 = 1$ as the dielectric and for a metal with negligible damping described by equation (2. 7), equation (2. 15) transforms into:

$$k = \frac{\omega}{c}\sqrt{\frac{\omega^2 - \omega_p^2}{2\omega^2 - \omega_p^2}} \tag{2. 16}$$

Figure 2.2 shows equation (2. 16) being plotted as a function of frequency ω normalized by ω_p. $\omega = ck$ is the light line, and the solid line to the right of it represents the SPPs being bound to the surface. The dispersion relation is:

$$\omega^2(k) = \frac{\omega_p^2}{2} + c^2 k^2 - \sqrt{\frac{\omega_p^4}{4} + c^4 k^4} \tag{2. 17}$$

We can thus see that in vacuum, for large wave-vectors, the frequency of the SPP is asymptotic to the non-dispersive surface plasmon frequency, $\omega_s = \omega_p/\sqrt{2}$.

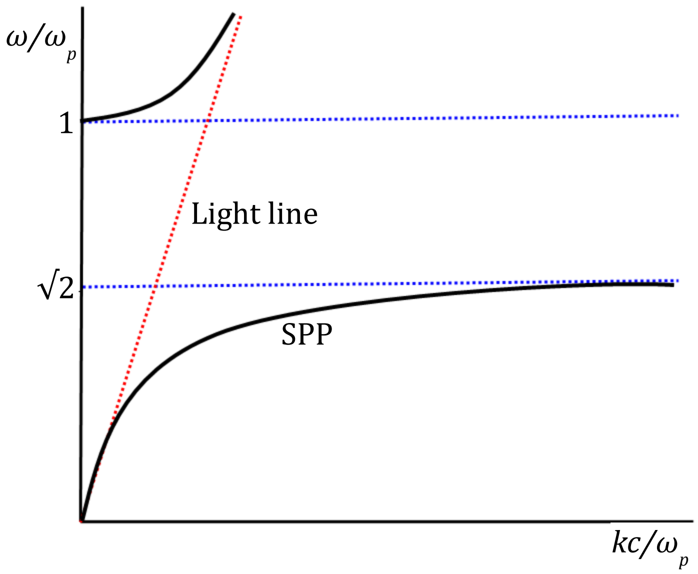

Figure 2.2: Dispersion relation of surface plasmons at a Drude metal-air interface.

For a flat interface, light impinging from the dielectric side will have a dispersion line above the light line and exciting SPPs will be impossible. To allow such external radiation to couple, surface roughness or grating are required to add an additional wave-vector component to the photons.[35-37] For a thin metal film, surface plasmons can be coupled on the air side through a high-index glass prism.

Now that it was seen how the problem of two semi-infinite media can be solved and leads to the localization of the electromagnetic field in one dimension, one can consider how to model conductive nanoparticles behaviour in an oscillating field.

2. 3 Localized surface plasmons

The detection of small changes in the wavelength position of LSPs in metal nanostructures has been used successfully in biosensing applications, such as label-free detection. The sensing principle is based on the plasmon resonance spectral shift caused by a change in the dielectric properties of the environment similar to the SPPs. LSPs allow real-time monitoring of molecular binding events using standard optical spectroscopy reaching as far as single-molecule detection.[38]

LSPs arise naturally in metallic nanostructures in an oscillating electromagnetic field. Similarly to surface plasmons, the electromagnetic field will drive the electrons. The curvature of the nanoparticle will exert an effective restoring force, creating a resonance at which point there will be amplification of the field both inside and in the near-field region outside of the nanostructure. The simplest case consists of a metallic particle whose dimensions are much smaller than the wavelength of light considered. This is the quasi-static approximation. It means that over the whole particle, there is no phase retardation of the harmonically oscillating electromagnetic field. One can thus derive formulas using an electrostatic field and add the time dependence afterwards.

Let's consider a sphere or radius a in a uniform electrostatic field $\boldsymbol{E} = E_0\boldsymbol{u_z}$. The particle, characterized by ε_1, is surrounded by an isotropic non-absorbing medium with dielectric constant ε_2. The applied field will induce a dipole moment, $\boldsymbol{p}$, proportional to the amplitude $|\boldsymbol{E_0}|$ such that $\boldsymbol{p} = \varepsilon_0\varepsilon_2\alpha\boldsymbol{E_0}$ with α being the polarizability of the particle. Doing the calculations would lead us to the following expression of the polarizability, which takes the form of a Clausius-Mossotti relation:[26]

$$\alpha = 4\pi a^3 \frac{\epsilon_1 - \epsilon_2}{\epsilon_1 + 2\epsilon_2} \tag{2. 18}$$

By replacing ε_1 with the Drude function, this point-like dipole would have its polarizability equal to:

$$\alpha = 4\pi a^3 \left(\frac{\omega_0^2}{\omega_0^2 - \omega^2 - i\gamma\omega} - \frac{(\omega^2 + i\gamma\omega)(1-\epsilon_2)/(1+2\epsilon_2)}{\omega_0^2 - \omega^2 - i\gamma\omega} \right) \tag{2. 19}$$

, with $\omega_0 = \omega_p/\sqrt{(1+2\varepsilon_2)}$. If the nanoparticle is in vacuum, $\varepsilon_2 = 1$, the polarizability becomes a Lorentzian with a resonance at $\omega_0 = \omega_p/\sqrt{3}$. From the more general equation (2. 18), it is clear that a resonant condition is reached for a minimum value of $|\varepsilon_1 + 2\varepsilon_2|$.[39, 40] The associated mode is called the dipole surface plasmon. We can also see that changes in the dielectric, such as an increase of the value ε_2, would make the resonance red-shifts. Such a sensitivity to the surrounding medium makes metallic nanoparticles good candidates as an optical sensing tool.[41]

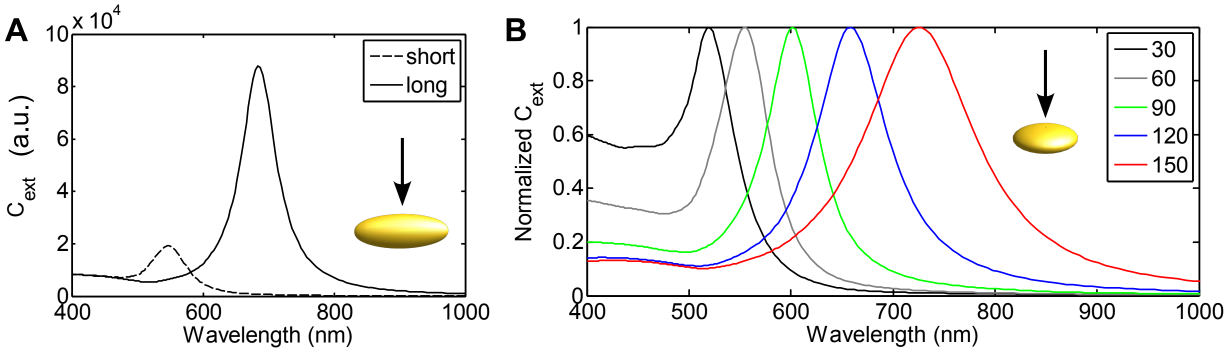

Figure 2.3: Point-dipole simulation of gold ellipsoids surrounded by a medium of refractive index $n = 1.25$ illuminated at normal incidence. (A)Anisotropic spheroid ($2a_1 = 120nm$, $2a_2 = 60nm$, $2a_3 = 30nm$) with the incident light polarization parallel to the long- (a_1) and short-axis (a_2), respectively. (B)Oblate spheroid with constant thickness $2a_3 = 30nm$ and for variable diameter $2a_1 = 2a_2 = 30\text{-}150nm$.

The optical cross-sections of a nanosphere surrounded by a dielectric medium are equal to:[39]

$$\begin{gathered} C_{sc} = \frac{k^4}{6\pi}|\alpha|^2 = \frac{8\pi k^4}{3} a^6 \left| \frac{\epsilon_1 - \epsilon_2}{\epsilon_1 + 2\epsilon_2} \right|^2 \\ C_{ab} = k\,\Im(\alpha) = 4\pi k a^3 \Im\left(\frac{\epsilon_1 - \epsilon_2}{\epsilon_1 + 2\epsilon_2} \right) \end{gathered} \tag{2. 20}$$

, with $C_{ext} = C_{ab} + C_{sc}$, where C_{ext}, C_{ab}, and C_{sc} are the extinction, absorption, and scattering cross-sections, respectively.

If we change the sphere to a more general geometrical shape, like an ellipsoid with semi-axis a_1, a_2, and a_3, then the expressions of the nanostructure polarizabilities along each axis are altered from equation (2. 18) to:[39]

$$\begin{gathered}\alpha_i = 4\pi a_1 a_2 a_3 \frac{\epsilon_1 - \epsilon_2}{3\epsilon_2 + 3\mathrm{L}_i(\epsilon_1 - \epsilon_2)} \\ L_i = \frac{a_1 a_2 a_3}{3} \int_0^\infty \frac{dq}{(a_i^2 + q) f(q)} \\ f(q) = \sqrt{(q + a_1^2)(q + a_2^2)(q + a_3^2)} \\ \sum L_i = 1 \end{gathered} \tag{2. 21}$$

, where *i = 1, 2, 3* denotes the direction along the different axis of the ellipsoid, and L_i are the depolarization factors. Usually nanodisks are modelled by an oblate spheroid for simplicity ($a_1 = a_2$, $a_1 > a_3$). Prolate spheroids ($a_1 = a_2$, $a_1 < a_3$), and anisotropic particles in general, are of interest due to their different resonances depending on the impinging light direction and polarization. For example, by illuminating an anisotropic nanoparticle, such as simulated in Figure 2.3A, at normal incidence, aligning the light polarization along the short-axis or long-axis of the particle will allow different resonances to be probed. The two peaks in the extinction cross-sections spectra are related to the two in-plane resonances. Gold nanorods and the dependence of their optical properties on their aspect ratio has been the subject of many studies.[42] It is observed that for an increasing aspect ratio, anisotropic nanoparticles see a small blue-shift of their transversal resonance and a strong red-shift of their longitudinal resonance.

Extending the model further, by including the field retardation effects and radiative damping, can become important for larger particles as it induces small spectral changes. The so-called modified long wavelength approximation (MLWA) takes them into account and has been introduced by M. Meier and A. Wokaun for a sphere,[43, 44] and by T. Jensen for an ellipsoid in the following expression:[45]

$$\alpha_{i,MLWA} = \frac{\alpha_i}{1 - \frac{k^2}{4\pi\epsilon_0\epsilon_2 a}\alpha_i - \frac{ik^3}{6\pi\epsilon_0\epsilon_2}\alpha_i} \tag{2. 22}$$

, where α_i is the quasi-static polarizability in the direction *i* of an ellipsoid of radii a_1, a_2, and a_3, from equation (2. 21). Following the MLWA, Figure 2.3B shows the extinction cross sections of gold ellipsoids of different diameters with constant thickness. As the diameter increases, there is a significant red-shift of the resonance position as well as a broadening due to the increase of the depolarization factor and radiation-damping.

When two or more nanostructures are brought together, they interact. Based on the point-dipole model introduced in this part, the coupled dipole approximation (CDA) can be used to describe the resulting behaviour.

2. 4 Interparticle coupling

The resonant wavelength of a metallic nanoparticle is known to be dependent on its size, shape, material, and surrounding medium. When several particles are brought together, such as in aggregated colloids, “hotspots” appear and the coupling between particles becomes very important. Near-field coupling effects will shift the plasmon resonant wavelength as a function of particle separation. Localized field enhancement in hotspots provides dramatic changes in the emission properties of fluorescent molecules and can lead to strong surface-enhanced Raman scattering (SERS).[45]

The coupled dipole approximation (CDA) is a simple model able to describe coupled plasmonic nanostructures.[44, 46, 47] Its main advantage relies in the speed at which it can perform calculations for a system composed of numerous nanoparticles. In this method, each nanoparticle is approximated by a point-dipole located at its centre of mass. Contrary to Mie theory, multipoles are not included in the interparticle interactions which causes the interactions to be underestimated for nanoparticles separated by close distances.

Each particle *j* that composes our system is assumed to be an ellipsoid and is associated with a polarizability following the MLWA. One can ascribe them to a diagonal polarizability tensor:

$$\begin{gathered}\tilde{\alpha}_{j,ii}=\alpha_{ii,MLWA}\\ \bar{\alpha}_j=\begin{bmatrix}\tilde{\alpha}_{j,xx} & 0 & 0\\ 0 & \tilde{\alpha}_{j,yy} & 0\\ 0 & 0 & \tilde{\alpha}_{j,zz}\end{bmatrix}\end{gathered} \tag{2.23}$$

, where $\alpha_{ii,\,MLWA}$ is the quasi-static polarizability of an ellipsoid according to equations (2. 22) along the axes $i = x, y, z$.

The CDA method is then based on solving the following equation:

$$\begin{gathered}\boldsymbol{p}_j=\bar{\alpha}_j\boldsymbol{E}_j=\bar{\alpha}_j\Big(\boldsymbol{E}_{inc,j}-\sum_{k\neq j}\boldsymbol{A}_{jk}\boldsymbol{p}_k\Big)\\ \boldsymbol{E}_{inc,j}=\boldsymbol{E}_0\exp\left(i\,\boldsymbol{k}\cdot\boldsymbol{r}_j-i\,\omega\,t\right)\end{gathered} \tag{2.24}$$

, where $\boldsymbol{p}_j$ represents the point-dipole located at positions $\boldsymbol{r}_j$ from the origin, and $\boldsymbol{E}_j$ is the local electric field. $\boldsymbol{E}_j$ can be decomposed into the incident plane-wave field, $\boldsymbol{E}_{inc,j}$, and the sum of the retarded induced dipole field, $-\boldsymbol{A}_{jk}\boldsymbol{p}_k$, by a particle *k* at a position *j*. $\boldsymbol{A}_{jk}$ is a 3x3 matrix for $j \neq k$:

$$\boldsymbol{A}_{jk}=\exp\frac{(ikr_{jk})}{r_{jk}}\times\Big(k^2(\hat{r}_{jk}\hat{r}_{jk}-\mathbf{1}_3)+\frac{ikr_{jk}-1}{r_{jk}^2}(3\hat{r}_{jk}\hat{r}_{jk}-\mathbf{1}_3)\Big) \tag{2.25}$$

, where $k \equiv \omega/c_0 n$, $r_{jk} = |\boldsymbol{r}_j - \boldsymbol{r}_k|$, $\hat{r}_{jk} \equiv (\boldsymbol{r}_j - \boldsymbol{r}_k)/r_{jk}$, $\boldsymbol{1}_3$ is the 3x3 identity matrix, and n is the surrounding medium refractive index. By defining $\boldsymbol{A}_{jj} \equiv \bar{\alpha}_j^{-1}$ the scattering problem reduces to a system of $3N$ complex linear equations, N being the total number of dipoles in the system:

$$\sum_{k=1}^{N}\boldsymbol{A}_{jk}\boldsymbol{p}_k=\boldsymbol{E}_{inc,j} \tag{2.26}$$

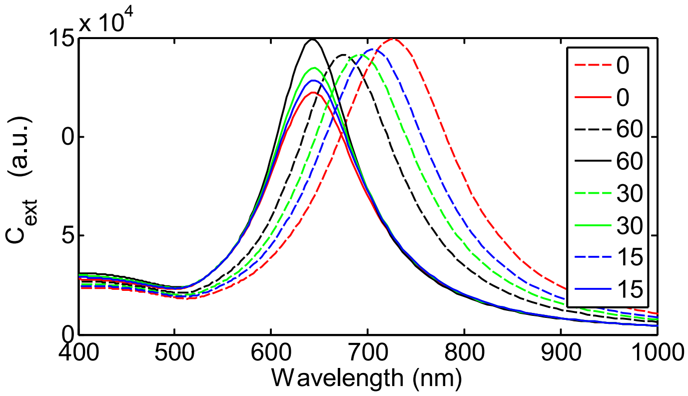

Figure 2.4: CDA calculations of a gold dimer in a surrounding medium with refractive index n = 1.25. The oblate spheroids ($2a_1 = 120nm, 2a_2 = 120nm, 2a_3 = 30nm$) separated by a gap $d = 0\text{-}60nm$ are illuminated by light whose polarization is perpendicular (solid lines) and parallel (dashed lines) to the dimer axis. As the gap decreases, the longitudinal and transversal modes shift to the red and blue, respectively.

Solving equations (2. 24) by direct matrix inversion gives the dipole moments of the nanoparticles, from which can be calculated the extinction, absorption, and scattering cross-sections according to:

$$\begin{gathered} C_{ext}=\frac{k}{|\boldsymbol{E}_{inc}|^2}\sum_{j=1}^{N}\Im(\bar{\boldsymbol{E}}_{inc,j}\cdot\boldsymbol{p}_j) \\ C_{ab}=\frac{k}{|\boldsymbol{E}_{inc}|^2}\sum_{j=1}^{N}\left(\Im(\boldsymbol{p}_j\cdot\bar{\alpha}_j^{-1}\bar{\boldsymbol{p}}_j)-\frac{2}{3}k^3|\boldsymbol{p}_j|^2\right) \\ C_{sc}=C_{ext}-C_{ab} \end{gathered} \qquad (2.\ 27)$$

When placing two point-dipoles next to each other, the dipole moment of each particle is the sum of the moment induced by the incident field and by the scattered field from the neighbouring particle. As a consequence, the dimer nanostructure will have different resonance conditions with respect to the individual single particles composing it. When illuminated at normal incidence with light polarization along the dimer axis, closing the gap in the dimer will decrease the restoring force inducing a red-shift of the resonance. When illuminated with light polarization perpendicular to the dimer axis, the opposite happens; the restoring force increases as the interparticle distance shortens resulting in a slight blue shift of the resonance. To illustrate this behaviour, two oblate ($2a_1 = 120nm, 2a_2 = 120nm, 2a_3 = 30nm$) gold spheroids have been modelled by CDA in a surrounding medium with refractive index $n = 1.25$. The gap distance, d, was varied from 0 to $60nm$, and resonances for perpendicular (solid lines) and parallel (dashed lines) light polarization have been computed. The results are displayed in Figure 2.4. Indeed, both red-shift from the longitudinal mode and blue-shift from the transversal mode happen, albeit being limited for the blue-shift.

It has been observed in literature that the CDA model underestimates interparticle interactions for close interparticle distances due to the omission of higher-order modes.[46] In the near-field interaction regime, higher-order multipoles must be included. A correction can be made for multipolar effects by making the spheroids boundaries overlap ($d < 0$).[47]

As the number of point-dipoles included in the system increases, one can transition to another model where the nanostructures are not considered individually but as a metasurface.

2. 6 Modified Fresnel coefficients

The samples usually prepared in our labs are based on the hole-mask colloidal lithography (HCL) method.[48] The lithography relies on the use of latex beads to create holes in the patterning mask. They can be viewed as two-dimensional arrays of nanoparticles. Due to the processing technique employed, the nanoparticles are placed randomly on a substrate with a typical interparticle average distance equals to 2-3 bead diameters. The array is characterized by a short-range order, which means that the nanostructures are weakly interacting with each other over long distances.[49] When light is impinging on the sample, a quasi-infinite number of dipoles scatter coherently. However, the optical response from the substrate surface musts not be neglected. As such, the metasurface composed by the nanostructures meta-atoms can be described by an effective refractive index of a two-dimensional interference phenomenon between the reflection from the substrate surface, and the reflectance from the nanostructures layer. Derived from Maxwell's equation using some specific boundary conditions, one arrives at a set of modified Fresnel coefficient to characterize the optical properties of the nanoparticles array.[50] Reports have been made in the literature about the use of the modified Fresnel coefficients as equivalent to the island film theory. It proved to be very useful in modelling the conditions to obtain total light annihilation from arrays of nanoparticles.[51]

As seen previously, it is reasonable to consider each nanoparticle as a point-dipole. If we deal with a layer of nanoparticles whose thickness is significantly smaller than their lateral dimensions, they can be approximated by a single interface and associated to a surface polarization which is the sum of the nanoparticles polarizabilities. In turn, the surface polarizability will modify the boundary conditions of equations (2. 9). To the picture of the two semi-infinite media depicted in Figure 2.1 musts be added a surface component at $z = 0$.

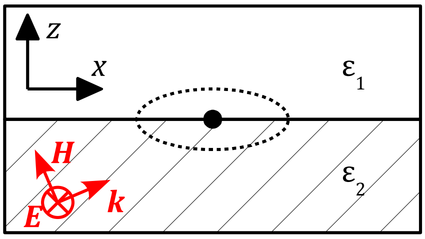

Figure 2.5: Schematic of an ellipsoid represented as a point-dipole positioned at the interface between two semi-infinite media *1* and *2*.

The electrical fields can be rewritten as $\boldsymbol{E}=\boldsymbol{E}_2\Theta(-z) + \boldsymbol{E}_{sur}\delta(z) + \boldsymbol{E}_1\Theta(-z)$, where Θ and δ are the Heaviside and Dirac delta functions, respectively. The modified boundary conditions for a non-magnetic system, may be written as:[50]

$$\begin{gathered}D_{1z}-D_{2z}=-\nabla_{\|}\cdot P_{\|}^{sur}\\ B_{1z}-B_{2z}=0\\ E_{1\|}-E_{2\|}=-\nabla_{\|}p_{z}^{sur}\\ H_{1\|}-H_{2\|}=i\frac{\omega}{c}z\times P_{\|}^{sur}\end{gathered} \tag{2.28}$$

, where the || index denotes the *xy*-plane. Skipping past the derivations following the modified boundary conditions, the modified Fresnel coefficients for nanodisks are given by the following equations:

$$\begin{gathered}r_p=\frac{E_p^r}{E_p^i}=\frac{n_t\cos\theta_i-n_i\cos\theta_t-i\frac{\omega}{c}\rho\alpha_{disk}\cos\theta_i\cos\theta_t}{n_t\cos\theta_i+n_i\cos\theta_t-i\frac{\omega}{c}\rho\alpha_{disk}\cos\theta_i\cos\theta_t}\\ r_s=\frac{E_s^r}{E_s^i}=\frac{n_i\cos\theta_i-n_t\cos\theta_t+i\frac{\omega}{c}\rho\alpha_{disk}}{n_i\cos\theta_i+n_t\cos\theta_t+i\frac{\omega}{c}\rho\alpha_{disk}}\\ t_p=\frac{E_p^t}{E_p^i}=\frac{2\mathrm{n}_i\cos\theta_i}{n_i\cos\theta_i+n_t\cos\theta_t-i\frac{\omega}{c}\rho\alpha_{disk}}\\ t_s=\frac{E_s^t}{E_s^i}=\frac{2\mathrm{n}_i\cos\theta_i}{n_t\cos\theta_i+n_i\cos\theta_t-i\frac{\omega}{c}\rho\alpha_{disk}\cos\theta_i\cos\theta_t}\end{gathered} \tag{2.29}$$

, where *p* and *s* denote the incident light polarization, *i*, *r*, and *t* denote the incident, reflected, and transmitted fields, respectively, ρ is the nanoparticles surface density, and α_{disk} is the in-plane polarizability of a disk modelled as an oblate spheroid. Detailed derivations can be found in the literature in the case of nanodisks, [50, 52] and in the Supplementary Material of Paper III in the case of a thin anisotropic ellipsoid. The strength of this model is in the resulting simplicity of its components where substrate and nanoparticles contributions can be separated. The nanoparticles are not considered individually any more but as an effective medium.

Chapter 3

Chirality

Symmetry is often associated with perfection and beauty. However, complete perfect symmetry (e. g. a sphere) is not present in nature. On the other hand, asymmetry plays a fundamental role in life and what surrounds us. From the shell of a snail, to the double helix of DNA, these examples (see Figure 3.1) illustrate a certain spatial organization. In 1904, Lord Kelvin gave a geometrical definition of chirality (see Chapter 1).[1] An especially notable example are our very own hands. Our right and left hands are mirror-images of each other; however, when superposed on each other they cannot be matched. Following their denomination one defines right-handed (RH) and left-handed (LH) enantiomers, according to their spatial organization, which are objects with opposite chirality.

From the very foundations of life, molecules give us innumerable examples of chirality. Almost all natural amino-acids are present as *L*-enantiomers, whereas all sugars are in the *D(R)*-configuration. Although many of their physical properties are identical, enantiomer molecules show stereo-selectivity. They are involved in chemical processes with molecules sharing the same handedness. As such, being able to distinguish between two enantiomeric forms is vital in the drug industry. Indeed, depending on its enantiomeric form, the same molecule can either be effective, or on the other hand present some secondary effects or no effect at all to treat some specific symptoms of a sickness. A tragic example is the one of the thalidomide. It was released as a painkiller drug and given to pregnant women to fight against morning sickness. Being a chiral molecule, when prepared in an achiral environment it has a 50% chance to be produced in either right- or left-handed configuration. What was distributed was a mix of both enantiomers. Although one handedness of the thalidomide acted as designed, the other handedness fixed itself on the DNA of the foetus inside the mother's womb. This caused different limbs malformations at birth for babies worldwide. Thalidomide is just one of the many examples when knowing handedness of a medication being produced is of vital importance.

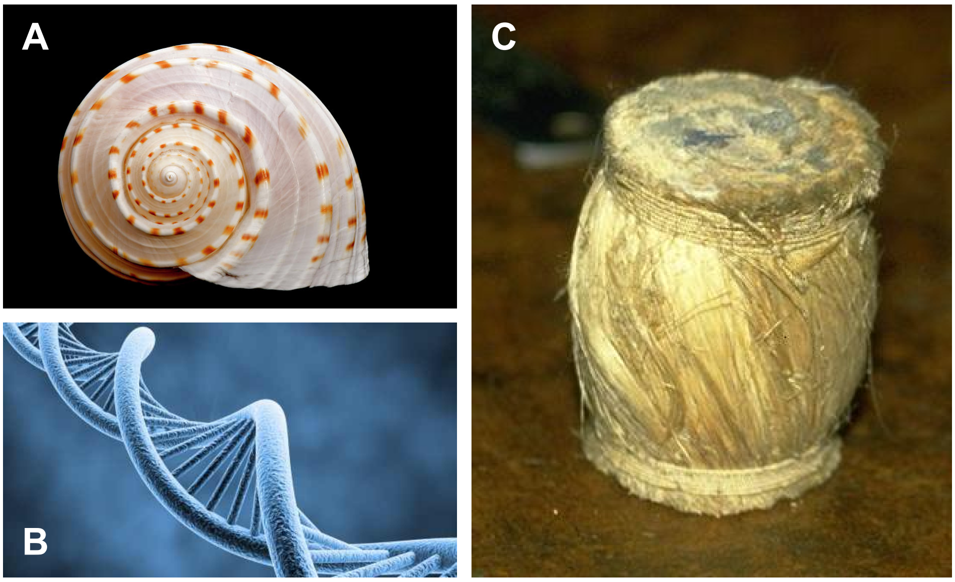

Figure 3.1: Chirality examples. (A)Spotted sea snail shell, (B)artist impression of a DNA double helix, and (C) one of the twisted-jute polarizers used by J. C. Bose.

The first technique developed to characterize molecular chirality was optical. Probing and comparing the interactions of a solution of molecules with left-handed circularly polarized light (LCP) and right-handed circularly polarized light (RCP) lead to the observation of a certain optical activity. Depending on the sign and amplitude of this optical activity, one would obtain a signature of the molecule geometry.

Materials ability to rotate light polarization was first demonstrated in quartz in 1811 by D. F. J. Arago.[53] and in 1812 by J.-B. Biot.[54] At that time, chirality was associated to the optical activity of the media, that is to say the rotation of the polarization plane of light as it goes through a 3D medium. A few years later, in 1815, J.-B. Biot showed polarization rotation in organic liquids such as turpentine and aqueous solutions of sugar. In 1825, Fresnel presented his theory of optical rotation preceded by his discovery of circularly polarized light.[55] It defined the optical activity as a consequence of circular birefringence for which different optical indices are ascribed to a certain medium for left- and right-handed circularly polarized light. Back in 1848, L. Pasteur studied how light polarization is affected by enantiomeric solutions of tartaric acid.[56] Enantiomers, chirality, and optical activity became then firmly linked. In 1874, J. A. Le Bel and J. H. van't Hoff managed to put together the relationship between optical activity and molecular structure, thereby starting the path of stereochemistry.[2, 3] Circular dichroism, the so-called Cotton effect,[57] circular birefringence, and optical activity came to be standard in the structural study of media and are very commonly used nowadays. But it is J. C. Bose in 1898, who after some experimentation with twisted bundles of jute, created artificial 3D-chiral structures able to modify the polarization state of *mm*-waves.

However, nowadays, advances in micro- and nanotechnology processing techniques allow an increased control in the patterning of nanostructures. This caused a renewed interest in the realization of metamaterials presenting optical activity. For instance, chiral metamaterials can be designed to obtain negative refractive index,[58] some achieve strong optical rotation,[59, 60] and three-dimensional chiral structures such as helices may be used as broadband circular polarizers.[61] But the most important is the possibility they offer to enhance the chiroptical effects of molecules through optical chirality.[62] In the following paragraphs I look over some of the recent developments in the field. In the first part a definition of different chiroptical effects is given, as well as what type of measurement can evaluate them. This is followed in a second paragraph by considerations on 3D helical- and tetrahedral-based chirality. The third paragraph is dedicated to another strategy to obtain chirality known as extrinsic chirality. In the last fourth part, superchirality is briefly discussed.

3.1 Chiroptical effects

Different chiroptical effects can be distinguished in organic molecules. Many of them are based on the tetrahedral bonding of the carbon atom. This bonding was uncovered by both A. Le Bel,[2] and J. H. van't Hoff.[3] In an achiral environment, formation of either enantiomeric form of a molecule has equal probabilities, and the energy needed to achieve either is also the same. Although chirality is more of a Boolean information, an object is either right-handed or left-handed, the chiroptical effects born from handedness are measurable and quantifiable informations. A chiral medium can be characterized optically by a refractive index, *n*, and an extinction coefficient, *k*. Of course for chiral media, both these quantities are altered for right- and left-handed circularly polarized light. The refractive index indicates how much the light speed is being reduced in a medium. The extinction coefficient shows how much the amplitude of the electromagnetic field, corresponding to the scattering and absorption of a material, is being affected by travelling through a substance. Linearly polarized light can be considered as the sum of a right- (RCP) and left-handed circularly polarized light (LCP)

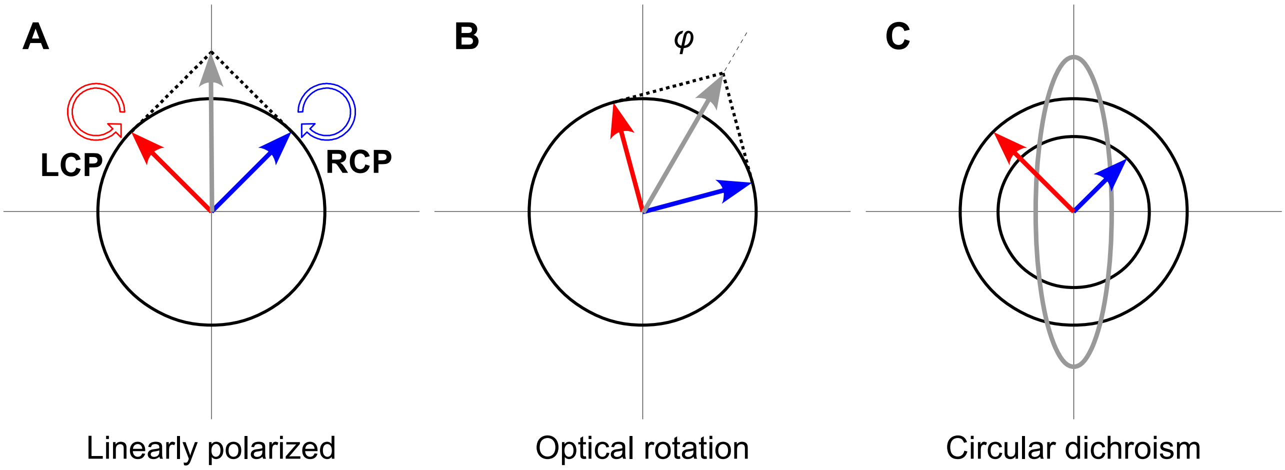

Figure 3.2: Chiroptical effects on linearly polarized light. (A)Linearly polarized light as the sum of a right- and left-handed circularly polarized light components of equal amplitudes. (B)RCP and LCP light experiences different phase velocities resulting in a rotation of the wave plane. This is the so-called *optical rotation*. (C)RCP and LCP light are scattered and/or absorbed differently resulting in an elliptical polarization state. This is the so-called *circular dichroism*.

components of equal amplitudes (as depicted in Figure 3.2A). If the refractive indices of the sample for LCP and RCP are different, when the components are recombined, the plane-polarized radiation will be rotated by an angle φ, as shown in Figure 3.2B. This effect is called optical rotation or circular birefringence. When characterizing a material optically as a function of wavelength, one measures the optical rotatory dispersion (ORD) and the angle φ is equal to:

$$\phi=\frac{\pi(n_{LCP}-n_{RCP})l}{\lambda} \tag{3. 1}$$

, where l is the path length through the material, and n_{RCP} or n_{LCP} represents the refractive index for right- and left-handed circularly polarized light, respectively.

In the case where the extinction coefficient is different depending on whether RCP or LCP light is propagating through the medium, the end result is different. Phase velocities for both handedness would be the same. However, scattering and absorption are altered depending on the light polarization. The two amplitudes of the linearly polarized light components are not equal any more upon exiting the material. When RCP and LCP light are now summed, the polarization state of the electromagnetic field is elliptical. It follows that this chiroptical effect is the so-called ellipticity, ε. When characterizing a material as a function of wavelength, one measures the difference in amplitude between RCP and LCP light and calculates a quantity called circular dichroism (CD):

$$CD(rad)=\tan\epsilon=\frac{I_{RCP}^{1/2}-I_{LCP}^{1/2}}{I_{RCP}^{1/2}+I_{LCP}^{1/2}} \tag{3. 2}$$

, where I_{RCP} or I_{LCP} is the light intensity that has passed through the medium upon illumination by RCP and LCP light, respectively.

Through both optical rotatory dispersion and circular dichroism, one can determine the chiral purity of a molecular solution. The sign of the CD determines the handedness of the different molecular branch elements. Enantiomeric forms of a molecule display opposite signals for ORD and CD. This property can be used to distinguish a true 3D chiral object. For a chiral object following the definition given by Lord Kelvin,[1] the system handedness should be the same from all angles. As a consequence, the CD spectra from two opposite directions of illumination should be identical. On the other hand, a 2D planar chiral system is defined as an object which cannot be superimposed with itself until left from the plane. When flipped, a 2D planar chiral system has its handedness changed. Thus, the flipped structure CD signal is the opposite as it was upon illumination from the initial orientation.

V. A. Fedotov *et al.* and A. Drezet *et al.* provided a good way to characterize different types of chiral media through the use of the Jones matrix.[63, 68] It has to be reminded that under the paraxial approximation, the properties of light going through a medium can be fully described and understood by defining a 2X2 Jones matrix, J, such that:

$$J=\begin{pmatrix} J_{xx} & J_{xy} \\ J_{yx} & J_{yy} \end{pmatrix} \tag{3. 3}$$

However, since a chiral media is considered here, it is more practical to have the Jones matrix in a circularly polarized light basis:

$$\bar{J}=\begin{pmatrix} J_{ll} & J_{lr} \\ J_{rl} & J_{rr} \end{pmatrix}=U\,J\,U^{-1} \qquad (3.\,4)$$
$$U=\frac{1}{\sqrt{(2)}}\begin{pmatrix} 1 & -i \\ 1 & i \end{pmatrix}$$

, where *U* is the unitary matrix to transform the linear basis. If the Lorentz principle is respected, one will arrive at the Jones matrix for the flipped medium. Flipping the medium can be done by a rotation by an angle *π* of the *yz*-plane around the *x*-axis. One thus obtains:

$$\bar{J}^{flip}=\begin{pmatrix} J_{ll} & J_{rl} \\ J_{lr} & J_{rr} \end{pmatrix} \qquad (3.\,5)$$

Getting back to the definition of chirality by Lord Kelvin and formulating it in terms of transformation matrices go as follows. What needs to be looked at are the optical characteristics of the medium, or sample, through a planar symmetry Π_η. The transformation matrix in circular polarization basis, corresponding to a mirror symmetry with respect to a symmetry axis at a *η/2* angle from the *x*-axis, is equal to:

$$\bar{\Pi}_\eta=\begin{pmatrix} 0 & e^{-i\eta} \\ e^{+i\eta} & 0 \end{pmatrix} \qquad (3.\,6)$$

Through the symmetry, the initial Jones matrix is transformed in the circular basis to:

$$\bar{J}_\Pi=\bar{\Pi}_\eta\cdot\bar{J}\cdot\bar{\Pi}_\eta^{-1}=\begin{pmatrix} J_{rr} & J_{rl}e^{-i2\eta} \\ J_{lr}e^{+i2\eta} & J_{ll} \end{pmatrix} \qquad (3.\,7)$$

Trying to follow Lord Kelvin's definition means that under mirror-symmetry, a non-chiral system should be invariant under the transformation. The initial Jones matrix and the transformed matrix should be equivalent. This condition is possible only if both following equalities are respected:

$$J_{ll}=J_{rr}$$
$$J_{rl}=J_{lr}e^{+i2\eta} \qquad (3.\,8)$$

It also means that now a definition in terms of Jones matrix elements to obtain optical chirality is reached:

$$J_{ll}\neq J_{rr}$$
$$|J_{lr}|\neq|J_{rl}| \qquad (3.\,9)$$

Optical chirality is obtained if either or both of these conditions are respected. From the aforementioned inequalities, three classes of chiralty can be distinguished.

I – $J_{ll} \neq J_{rr}$ and $|Jl_r| = |J_{rl}|$. This corresponds to the class usually being denominated 3D chiral.

II – $J_{ll} = J_{rr}$ and $|Jl_r| \neq |J_{rl}|$. The nanostructures belonging to this class are generally 2D chiral.

III – $J_{ll} \neq J_{rr}$ and $|Jl_r| \neq |J_{rl}|$. It is the more general case of chirality.

In the following paragraph, I discuss about chiral plasmonic structures whose geometries take example on naturally chiral systems such as the DNA helical shape, and the tetrahedral conformations around a carbon atom.

3. 2 Helical and tetrahedral chirality

The first strategies developed in chiral nanostructuring can be linked to the ones adopted by chiral molecules and biological systems. The clearest example of three-dimensional chirality might be a simple helix and is copied from the DNA double helix representation.

An intuitive explanation of what happens when circularly polarized light impinges on a plasmonic structure can be given starting from Figure 3.3. As explained in Chapter 2, an electromagnetic wave drives electron cloud oscillations at the surface of a plasmonic nanoparticle. In the case of circularly polarized light impinging on a nanosphere, the electron cloud moves and describes a spiral. Circulation of the electrons gives rise to an electric current as they spiral around the sphere. For a metallic helix, the handedness could create a surface current along or against the metallic helix own handedness.

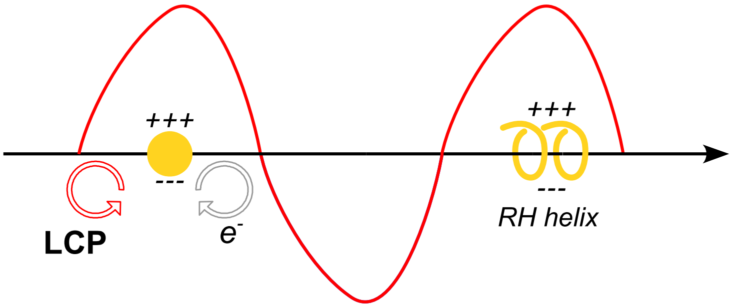

Figure 3.3: A metallic nanosphere and a right-handed helix excited by LCP light. As the light propagates, the electron cloud is being driven in a spiral manner. There is no difference from the point of view of the nanosphere whether the light polarization is right- or left-handed. However the surface current circulation can be hindered depending on the helix handedness with respect to the one of the impinging light.

The first strong chiroptical signals from plasmonic nanostructures were reported for gammadion structures.[60] In that article, 2D gold nanostructures capped by chromium showed circular dichroism stronger than chiral molecular media with an equivalent thickness. It inspired several other articles as a base for enantiomer sensing,[62] as well as optical rotation[64], and breaking of time-reversal symmetry.[65] However, it created a debate as to what is planar chirality.[65-67] Indeed, from a geometrical point of view, the structures themselves are two-dimensional and as such the circular dichroism spectra measured from opposite direction of illumination should be mirrors of each other. In reality, the gammadion samples displayed similar CD spectra from front and back illumination. As a consequence, something had to break the symmetry in a third dimension for the chirality definition to be consistent. The conclusion reached was that the chromium capping on one side and the substrate presence on the other side created two asymetrical interfaces.

More definite three-dimensional nanostructures taking the shape of helices were studied and produced.[69-74] Most of these examples are systems fabricated from a bottom-up approach by adding gold nanoparticles to an already chiral template. This method is the closest to being used in “real” applications as it is faster, cheaper, and easier to mass-produce than a top-down approach. However, their design is quite limited for now compared to the flexibility of patterns offered by lithography techniques. All the examples mentioned are composed by simple colloidal particles and the final dimensions of the chiral objects in solution are hard to control in a reliable way to produce a mono-disperse sample.

Another typical architecture used in three-dimensional chiral systems is the tetrahedron. It is inspired by the tetrahedral bonding structure stemming from carbon chiral centres. Two paths are possible when adopting a tetrahedral shape as seen in Figure 3.4. Symmetry can be broken by designing a tetrahedron with an asymmetrical structure but with identical components. This is called constitutional chirality. It is the preferred design for plasmonic three-dimensional chiral nanostructures.[69, 77, 78] The reason for that is quite simple. Indeed, as the plasmonic elements are of the same dimensions, coupling occurs easily. On the other hand if the structure geometry is achiral as in the case of compositional chirality, the symmetry breaking will originate from the choice of elements with different “weights”.[69, 77, 79, 80]

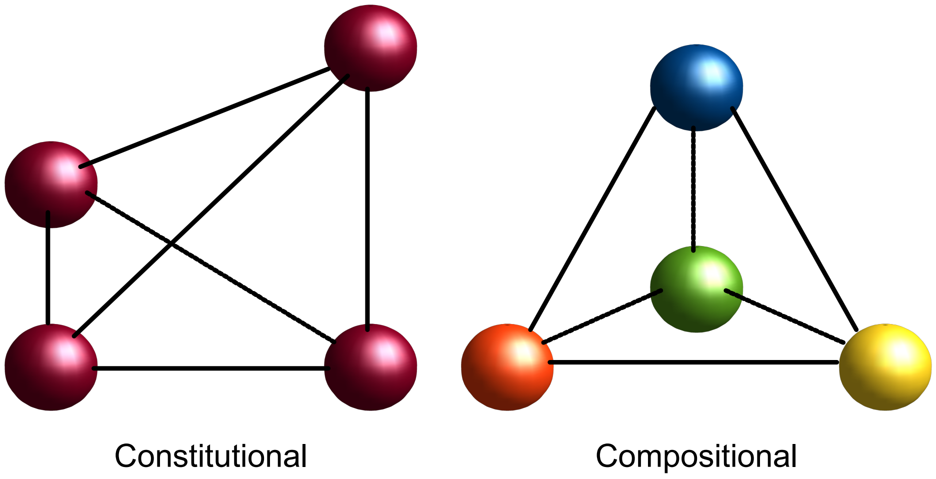

Figure 3.4: Illustration of two different approaches to tetrahedral chirality: from the geometry of the structure (constitutional chirality), or from the unbalance between the elements of the structure (compositional chirality).

It is generally accepted that constitutional chirality can offer a higher optical activity than compositional chirality.[77] It can be explained as follows. Upon interaction with the incoming circularly polarized light, the resonant gold particles couples efficiently. Real currents flowing in each particle are excited, as well as currents between the coupled elements. Due to the shape asymmetry, the displacement currents follow a helical movement, which induces a magnetic moment with some component parallel to the electric field dipole moment. The result is a strong structural signature in the circular dichroism spectrum. In contrast, the geometry of compositional chirality is achiral and the four plasmonic particles have weak resonant coupling; resulting in a weak optical activity. It is reported that constitutional chirality is very sensitive to dimension variations, both in particle size and interparticle distance.[80] Moreover, high-order multipoles have an important role to completely describe chirality in plasmonic oligomers.

However, design and production of true three-dimensional structures is difficult due to the high number of parameters that can be optimized as well as the sensitivity of the optical activity to dimension intolerances. A “simpler” architecture could be achieved by using extrinsic chirality.

3. 3 Extrinsic chirality

Similarly to the examples seen previously, chiroptical effects can be obtained from achiral objects by playing with the incident angle of light. Such an effect was first reported for parabola shaped elements in 2011 [81] and described for anisotropic thin films in 1996.[89] The overall tactic to achieve optical activity is common to many other articles[76, 81-89]. As seen in Figure 3.5A, the “trick” is to incorporate the light illumination direction in the chiral triad. Starting from an anisotropic 2D nanostructure, an elongated gold nanoparticle in the case of Paper III, the symmetry is broken in one dimension. When illuminated at an oblique angle, non-coincident to the two planes of symmetry of the nanoparticle, the system wave-vector/nanoparticle constitutes a three-dimensional chiral object.

Extrinsic chirality was achieved in many wavelength ranges, such as in the gigahertz,[87], in the mid-infrared,[83, 86] and in the visible.[82, 85, 88] Different mechanisms were used to explain the origin of the optical chirality shown by intrinsically achiral samples. Some structures, such as split-rings,[87] possess at the same resonance wavelength both an electric and magnetic response. Second-harmonic generation was also proven to be efficient in producing optical activity.[81, 89] Overall, anisotropy in either nanostructure or position of the meta-atoms is sufficient when associated to oblique incidence of the light wave-vector.

Extrinsic chirality displays several advantages over intrinsic chirality. As seen in the previous paragraph, coupling between the different elements of the three-dimensional chiral nanostructure and interparticle distance are crucial. On the other hand, extrinsic chirality is less sensitive to local structural details and imperfections in individual meta-atoms. Additionally, the strength of the CD signal can be modulated by the angle of incidence and the two “enantiomers” of a specific structure can be obtained from the same sample by mirror-tilting with respect to an in-plane axis of symmetry of the metasurface. This last property of extrinsically chiral system is displayed in Figure 3.5B where the reflection coefficient R_{LL} and R_{RR} are mirror images of each other.

However, the chiroptical effect shown by extrinsic chirality has to be differentiated from two-dimensional chirality. Indeed, a 2D chiral system is defined as an object which cannot be superimposed with itself until left from the plane. As a consequence, it doesn't have the optical activity signature expected for a 3D chiral object. Typical structures used for planar chirality are the Archimedean spiral,[92] the fishscale pattern,[63] or the gammadion.[62] The gammadion here is a bit of an exception as it shows pronounced optical activity. Additional symmetry breaking comes from the substrate presence. The polarization effect observed in the case of 2D chiral nanostructures differs with respect to the more common optical activity. Indeed, the effect is asymmetric in transmission with respect to the propagating wave direction.[63] The transmission and retardation of a circularly polarized wave are different in opposite directions. This is due to the fact that the planar chirality phenomenon is linked to a conversion of the impinging light handedness into light with the opposite handedness. When one changes the direction of propagation (or when the light polarization changes), the efficiency of the conversion is modified. When looking at the two non-diagonal elements displayed in Figure 3.5B, one can see that they are identical. Polarization conversion is not the main mechanism at play here. This is proof of the distinction between two-dimensional chirality and extrinsic chirality as discussed in the chirality categories defined via the Jones matrix.

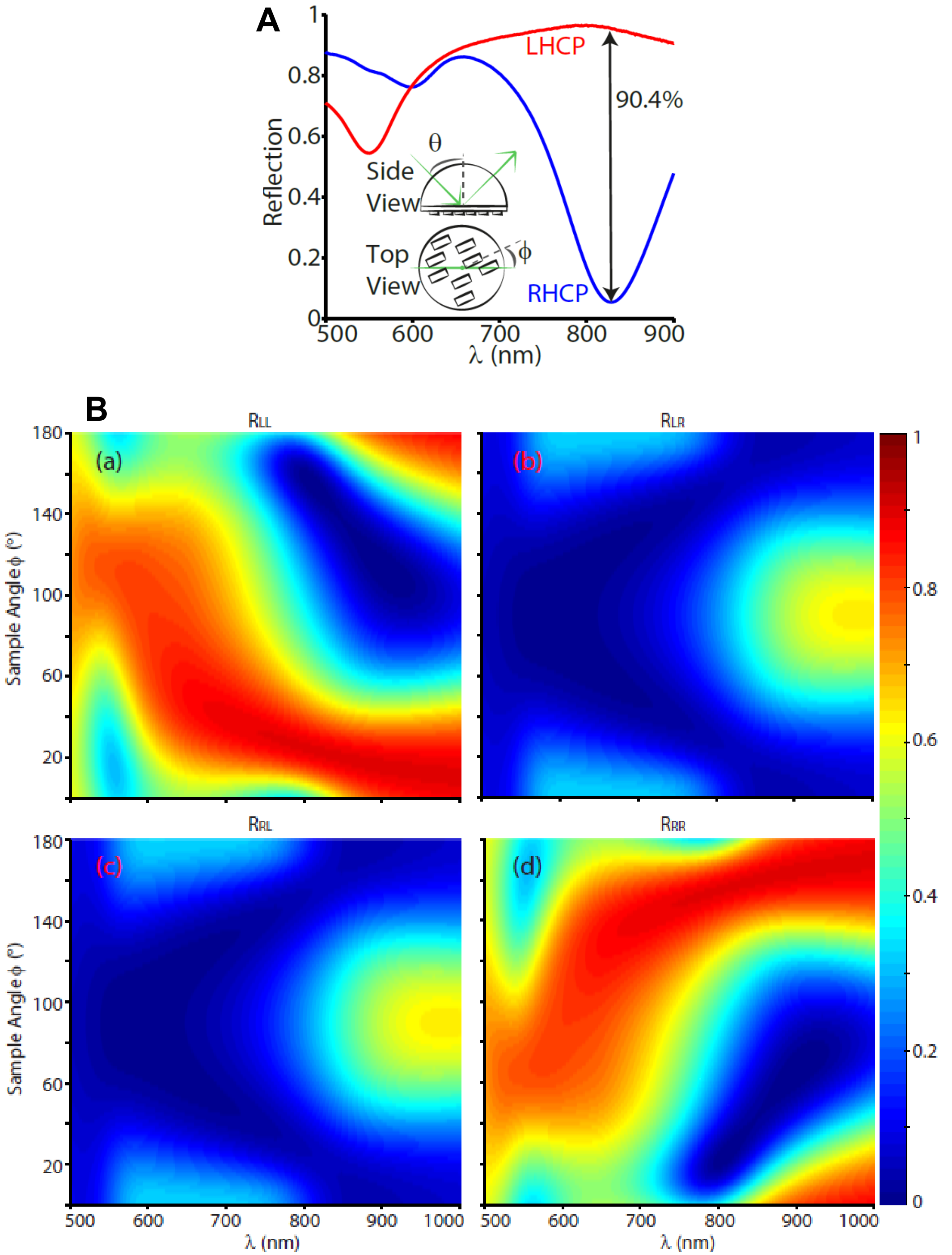

Figure 3.5: Extrinsic chirality example from Paper III. (A)Reflection measurements from an array of anisotropic gold nanoparticles, under RCP and LCP illumination, at $\theta_i = 45°$ and optimal sample orientation $\phi = 25°$. The insets define the incidence angle θ_i and the nanoparticle orientation ϕ. (B)The reflected intensity of the co- and cross-circular polarization components at $\theta_i = 45°$ and varying ϕ. The surface is illuminated with either (a-b) LCP or (c-d) RCP light and the output is divided into (a,c) LCP and (b,d) RCP light. (ex: R_{RL} is the LCP reflected intensity for a incident RCP light)

3. 4 Superchirality

The so-called superchirality is a value that can be calculated at each point in space linked to the intensity of a local chiral field. It has been proposed as a way to estimate the enhancement of the circular dichroism for biomolecular sensing by Y. Tang and A. E. Cohen.[90] Enantioselective signals are typically quite small. At the scale of a molecule, for the chiroptical effect to be at its maximum, it would be preferable to have the helical pitch of circularly polarized light to be in the same dimension range. Matching the light helical pitch with plasmonic nanostructures is more easily achievable. Thus it was hypothesized that, as plasmonic local field enhancements can be used to increase the interaction between light and the electronic, vibrational, and rotational resonances of molecules, superchiral electromagnetic fields would enhance interactions with chiroptical resonances of molecules.

The optical chirality, C, was defined originally by D. M. Lipkin as:[97]

$$C=\frac{\epsilon_0}{2}\boldsymbol{E}\cdot(\nabla\times\boldsymbol{E})+\frac{1}{2\mu_0}\boldsymbol{B}\cdot(\nabla\times\boldsymbol{B}) \tag{3. 9}$$

, where ε_0 and μ_0 are the permittivity and permeability of free space, respectively, and $\boldsymbol{E}$ and $\boldsymbol{B}$ are the local electric and magnetic fields. Y. Tang and A. E. Cohen main result is the proportional relation between the optical chiral asymmetry of a small molecule and the product of the chirality of matter and the chirality of the electromagnetic field.[90] To determine the enantioselectivity of a system, they consider the dissymmetry factor, g, which represents the difference in the rates of excitation between left- and right-handed circularly polarized light. The dissymmetry factor is defined by:

$$g=g_{CPL}\left(\frac{cC}{2\omega U_e}\right) \tag{3. 10}$$

, where g_{CPL} is the dissymmetry factor for a circularly polarized light plane-wave, c is the speed of light, and U_e is the local time-averaged electric energy density. From this equation, one can deduce that to enhance the enantioselective factor, the field chirality term (in parentheses) may be increased by increasing the optical chirality, C. Chiroptical effects, such as circular dichroism and optical rotation, may be an indication of local fields with enhanced optical chirality. From literature, the main contributions to superchirality come from electric dipole-magnetic dipole interactions and electric dipole-electric quadrupole interactions.

Biomolecular media were used in conjunction with plasmonic nanoparticles to create chiroptical effects.[91, 93-96] When light interacts with this kind of system, absorption occurs from the dissipative property of the molecular medium and from the optical chirality that interacts with the molecular medium. Thus, the final CD has contributions from both. The latter contribution is proportional to the difference in optical chirality between RCP and LCP illumination. It is usually more convenient to choose a system where the biomolecular medium and the plasmonic nanostructure are weakly interacting as it is easier to predict the enhancement from the sole study of the plasmonic part of the assembly. If the system is strongly interacting, that is to say when the plasmon resonance of a nanostructure and the molecular resonance are close, a

Fano-like effect will appear leading to an unpredictable CD signal.[96]

Chapter 4

Optical Trapping of Plasmonic Nanoparticles

Optical trapping, or optical tweezing, relies on the ability of light to apply a force on matter via transfer of momentum. One of the first observations of the mechanical interaction of light with objects dates back from a report by J. Kepler in 1619.[13] J. Kepler proposed that the reason why comets' tail are pointing away from the sun is because of the light pressure exerted by it. It is only much later, in 1901, that both P. N. Lebedev and E. F. Nichols and G. F. Hull showed experimental evidence of the light radiation pressure on the displacements of a torsion balance.[98, 99] Optical tweezing in its modern form was developed more than 45 years ago by A. Ashkin and coworkers. A. Askin *et al.* first demonstrated in 1970 how a focused laser beam could accelerate the motion of microparticles in liquids and gas,[100] and in 1971 how a micrometer-sized glass sphere could levitate in air.[101] But it is in 1986 that what would be called optical tweezers were born.[14] This technique allowed A. Ashkin and coworkers to trap in three-dimensions micro- and nanoparticles in water with a single-beam gradient force trap. Since then, optical tweezers became a classical optical manipulation tool and found applications in chemistry, biology, and physics. It enabled the application and detection of forces to micro- and nanoscale objects including single molecule chemistry

Figure 4.1: Photograph of the Hale-Bopp comet. Two tails are visible. Both the dust tail (in white) and the ions tail (blue) are pushed away by the sun light.

experiments.[102, 111]

For a dielectric particle, optical trapping originates from the radiation pressure applied by a focused laser beam. The particle absorbs and scatters photons and is pushed in the light direction due to the conservation of momentum. At the same time, there is a gradient force pulling the particle towards the highest intensity region. The gradient force dominates light interactions with particles in the case of dielectric material. On the other hand, plasmonic nanoparticles strongly absorb and scatter light close to their LSP resonance. Thus the scattering force becomes more important, and stable trapping is jeopardized. This provoked the development of new techniques for the trapping of metal nanoparticles.[17, 103, 104] From there on, optical trapping of plasmonic nanoparticles developed greatly. Theoretical works developed different models to derive optical forces on single particles and nanoaggregates.[105-108] Observation and analysis of trapped nanoparticles needed new spectroscopy methods.[109, 110] Not only spherical particles, but also nanoprisms, nanorods, and bipyramids were manipulated in optical trapping experiments.[112-115] Of course, optical trapping and the properties of plasmonic nanoparticles to enhance the electromagnetic fields were used in applications such as enhanced Raman scattering,[116] integrated in microfluidic environments,[117] and employed in nanofabrication.[106, 118] The latest progresses in optical manipulation go beyond conventional optical trapping and explore plasmonic optical trapping.[111, 119-128] Plasmonic optical tweezers allow for parallel trapping of nanoscale objects and can overcome the diffraction limits of conventional optical tweezers. The current performances are in the range of the piconewton detection. Current nanofabrication techniques can simplify their integration on lab-on-chips. However, plasmonic optical trapping is only in the proof-of-principle stage and future research is needed to push it further.

In this thesis, I want to focus on the rotation of nanoparticles in optical traps.[129, 130]. Applications spread from propulsion at the nanoscale,[131] to nanofluidic actuators.[132] In the first paragraph of this chapter I consider the different forces acting on nanoparticles in optical traps. It is followed in a second part by a description of the optical trapping setup and the means of detection of the nanoparticle motions. The third paragraph is dedicated to results on an on-going experiment, which consists in the trapping and rotation of a gold nanorod at the interface between vegetable oil and water.

4. 1 Optical forces on plasmonic nanoparticles

A nanoparticle whose dimensions are much smaller than the wavelength of the trapping laser can be represented as one or multiple dipoles. As seen in Chapter 2, the polarizability of a dipole expresses its interaction with an electromagnetic field. For an assymetric particle with polarizabilities α_{0x} and α_{0y} along the major axis in a plane perpendicular to the propagation direction of the incident light, the radiation reaction modifies the full polarizabilities from equation (2. 22).[130, 133]

The time-averaged force acting on such a dipole is:[134]

$$\langle \boldsymbol{F} \rangle = \frac{1}{2} \Re \left(\sum_j \alpha_{0j} E_j \nabla \bar{E}_j \right) \qquad (4.\ 1)$$

, where *j = x, y, z*, and **E** is the incident field. Equation (4. 2) can be rewritten to be split into two main components, the gradient force and the scattering force:[135]

$$\begin{gathered}\langle \boldsymbol{F}_{grad}\rangle = \frac{1}{4}\Re(\alpha_0)\nabla|\boldsymbol{E}|^2 \\ \langle \boldsymbol{F}_{sc}\rangle = \frac{\sigma_{ext}}{2\mathrm{c}}\Re(\boldsymbol{E}\times\bar{\boldsymbol{H}}) + \frac{\sigma_{ext}c\,\epsilon_0}{4\omega i}\nabla\times\boldsymbol{E}\times\bar{\boldsymbol{E}}\end{gathered} \tag{4. 2}$$

, where σ_{ext} is the extinction cross-section. The gradient force originates from the gradient of the intensity profile of the trapping laser. The scattering force represents the momentum transfer from the external radiation field to the nanoparticle by absorption and scattering. It is divided into two components: one proportionnal to the Poynting vector and in the direction of light propagation, the second from spatial polarization gradients.

The time-average torque applied to the particle along the propagation direction can be calculated as:[136]

$$M_z = \frac{1}{2}\Re(\bar{\boldsymbol{p}}\times(\boldsymbol{\alpha_0}^{-1}\boldsymbol{p})) \tag{4. 3}$$

, where **p** is the particle dipole moment. With an incident eletric field of amplitude E_0, an incident circularly polarized light can be written $\boldsymbol{E} = (\boldsymbol{u}_x + i\boldsymbol{u}_y)E_0/\sqrt{2}$, and keeping terms up to order k^3, the torque can be written:

$$M_z \approx \frac{E_0^2}{4}[\Im(\alpha_{0x}+\alpha_{0y}) + \frac{k^3\sqrt{\epsilon}}{6\pi\epsilon_0}\Re((\alpha_{0x}-\bar{\alpha}_{0y})\alpha_{0x} + (\alpha_{0y}-\bar{\alpha}_{0x})\alpha_{0y})] \tag{4. 4}$$

The first term of this last equation represents the torque related to light absorption. The second represents scattering contributions. So if we consider a non-absorbing asymmetric nanoparticle, the first term will vanish, and the torque can be simplified to:

$$M_z \approx \frac{E_0^2 k^3\sqrt{\epsilon}}{24\pi\epsilon_0}(\alpha_{0x}-\alpha_{0y})^2 \tag{4. 5}$$

When the dipole approximation is not valid any more, the time-averaged radiation force on a particle due to harmonic fields can be calculated by integrating the Maxwell stress tensor, **T**, over a closed surface, *S*, surrounding the particle:

$$\langle \boldsymbol{F}\rangle = \int_S \langle \boldsymbol{T}\rangle\cdot d\,\boldsymbol{S} \tag{4. 6}$$

, where ***dS*** is an infinitesimal surface element oriented perpendicular to the surface area. The time-averaged torque on the centre of mass of the particle can be calculated very similarly by:

$$\boldsymbol{M} = -\int_S \langle \boldsymbol{T}\rangle\times\boldsymbol{r}\cdot d\,\boldsymbol{S} \tag{4. 7}$$

, where ***r*** is the position of the element of surface area. The Maxwell´s stress tensor can be obtained from the total fields around the particle.

When rotating around a single axis, a particle driven by an external torque, M_{ext}, has its displacement following the equation of motion:

$$J\frac{d\omega}{d\tau}=M_{ext}+M_f+M_s \tag{4. 8}$$

, where J is the moment of inertia of the nanoparticle, ω is the instantaneous angular velocity of rotation, M_f is a friction torque proportional to ω, M_S is a stochastic torque. For a light intensity I, photon energy $\hbar\omega_0$, and a particle absorption cross-section σ_{abs}, the external torque due to spin angular momentum transfer is $M_{abs} = I\,\sigma_{abs}/\omega_0$.[137] On an asymmetric nanoparticle, scattering also induces an optical torque. By calculating the total optical torque from equation (4. 6), the optical torque scattering contribution can be obtained from $M_z = M_{sc} + M_{abs}$.

The viscous frictional torque is linked to the dynamic viscosity, η, of the liquid and follow Stokes equation for a laminar flow (low Reynolds number):[138]

$$M_f=-\pi\eta L^3\omega\gamma \tag{4. 9}$$

, where L is the length of the asymmetric nanoparticle modelled as a prolate spheroid, and γ is a geometrical factor depending on the spheroid eccentricity.[139] When a steady state is reached, the optical and frictional torques balance each other, which yields an average rotational frequency:

$$f=\frac{M_z}{2\pi^2\eta\gamma L^3} \tag{4. 10}$$

, where D is the short axis diameter of the prolate spheroid. Finally, the frictional torque in water can be influenced by the heating of the nanoparticle and an increase in temperature:

$$\eta(T)=\eta_0\exp[\frac{E_a}{N_A k_B(T-T')}] \tag{4. 11}$$

, where η_0 = 24,2 µPa.s for water, E_a = 4,74 kJ/mol is an activation energy, k_B is Boltzmann's constant, N_A is Avogadro's number, and T'= 140 K is a temperature offset. The temperature also influences the nanoparticle motion via a stochastic torque. This causes fluctuations in the angular velocity by an amount of the order of $(k_B\,T/J)^{1/2}$. The inclusion of the fluctuations due to Brownian motion in the signal analysis of a nanoparticle rotation is shown in the next paragraph.

4. 2 Optical trapping setup

Optical trapping of plasmonic nanoparticles is usually done by employing a laser wavelength detuned to the red with respect to the particle LSP resonance.[113, 115] The reason can be quickly deduced from looking at equation (4. 3). The gradient force on the blue side of the LSPR would be negative, meaning that the gradient force would be repulsive. However, close to the resonance, a strong scattering force dominates and pushes the nanoparticle in the light propagation direction, thus preventing three-dimensional trapping. Two-dimensional trapping is still possible by using a physical interface perpendicular to the direction of propagation to stop the motion of the nanoparticle. All of the optical trapping experiments I conducted so far were in a 2D trapping scheme depicted in Figure 4.2A.

The optical tweezers are built around an inverted microscope (Nikon TE300), and equipped with white-light dark-field illumination from a halogen lamp for the localization of the particles. A near-infrared laser (λ = 830nm) is the source of the trapping beam. Starting from the laser, the beam passes through a laser-line filter and a beam expander to obtain a light beam filling the back aperture of the objective. The light beam polarization is modified first by passing through a linear polarizer before passing through a quarter-wave plate to become circularly polarized. It is then reflected by a dichroic beamsplitter and focused by an air objective (60X; NA=0.7) to trap the gold colloids. The scattered light from the colloids from dark-field illumination (dark-field condenser; NA = 1.2-1.43) is collected by the objective, passes through a dichroic beamspliter and a hot mirror to remove contributions from the laser light, and is collected by a fibre-coupled avalanche photodiode (APD) before being analysed by an autocorrelator (ALV-5000). A linear polarizer can be placed in front of the fiber to measure the spinning frequencies of asymmetric nanoparticles.

The sample consists of a droplet of ~3μL of diluted colloidal suspension placed between two glass slides separated by a 100μm spacer. During the trapping experiment, the laser focus is moved slowly upward so that a trapped nanoparticle would be pushed and immobilized against the top glass slide. In that position, data is acquired by the APD using a 1s acquisition time. The autocorrelation function analysed is plotted in Figure 4.2B for a gold nanorod trapped against the glass interface at a laser power of 2.5mW with linearly and circularly polarized light, respectively. The autocorrelation function allows to distinguish between the different contributions to the intensity variations. It measures the correlation of a signal with itself shifted in time by some delay. The function is expressed as following:

$$C(\tau)=\frac{1}{t-\tau}\int_{0}^{t-\tau} x(t)x(t+\tau)\,dt \tag{4. 12}$$

, where τ is a time delay, and $x(t)$ is a signal. For circularly polarized light, the autocorrelation can be fitted to:

$$C(\tau)=I_0^2+\frac{I_1^2}{2}\exp(-\tau/\tau_0)\cos(4\pi f\tau) \tag{4. 13}$$

, where I_0 is the average intensity, I_1 is the amplitude of the intensity fluctuation as a result of the nanorod rotation, and τ_0 is the autocorrelation decay time due to the stochastic motion of the nanoparticle.

$$\tau_0=\frac{\pi\eta\gamma L^3}{4\mathrm{k}_B T}=\frac{\beta J}{N^2 k_B T} \tag{4. 14}$$

, where N is the symmetry order of the trapped object, and β is the velocity damping rate.

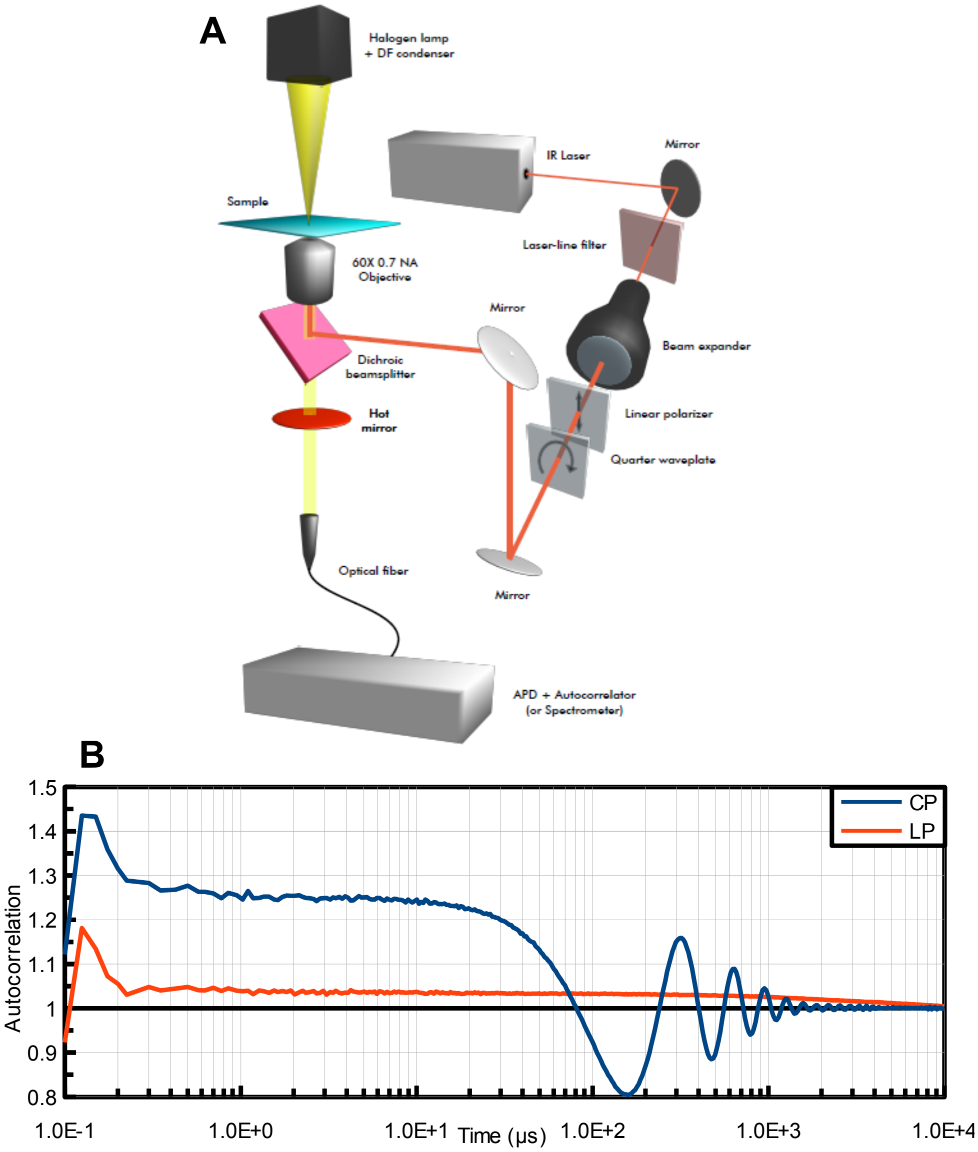

Figure 4.2: (A)Schematic of the optical trapping setup. (B)Representative autocorrelation function of a gold nanorod (*L* 190nm x *D* 120nm) trapped by a laser (830nm) with linearly (LP) and circularly (CP) polarized light at a power of 2.5mW.

From the graph in Figure 4.2B it is clearly seen that under illumination by circularly polarized light the nanorod is set in rotation and produces an oscillating autocorrelation function. Whereas a linearly polarized light illumination leads to an exponential decay and an alignment of the nanorod long axis along the polarization direction.[113, 115]

4. 3 Nanorod trapping at an oil-water interface

Disclaimer: The following paragraph is a compilation of results on an on-going project. Data is still lacking to have a complete understanding of the phenomena at play. It is in our intention to publish an article based on the data herein reported.

Liquid-liquid interfaces, and more particularly oil-water interfaces, are systems very important in the food and cosmetics industries because of the wide-spread use of emulsions.[140, 141] Behaviour and self-assembly of colloids at oil-water interfaces is of utmost importance for the understanding of problems like self-cleaning surfaces, drug delivery, emulsion formation and stability, and nanofabrication relying on colloidal self-assembly.[141-144] Detection of the relative position of a nanoparticle at an interface,[143, 145] as well as the interacting forces at play are investigated in the literature and are of high current interest.[146-152] In this framework, optical tweezers present themselves as a powerful tool for the mechanical probing of oil-water interfaces.

Similarly to a previous paper,[130] I chose to work with gold nanorods with lengths of around 190nm and diameters of 120nm because of their asymmetry and strong light scattering. Transfer of spin angular momentum then occurs with a reduced contribution from absorption, and thus less heating. The optical properties of the monocrystalline gold nanorods are displayed in Figure 4.3.

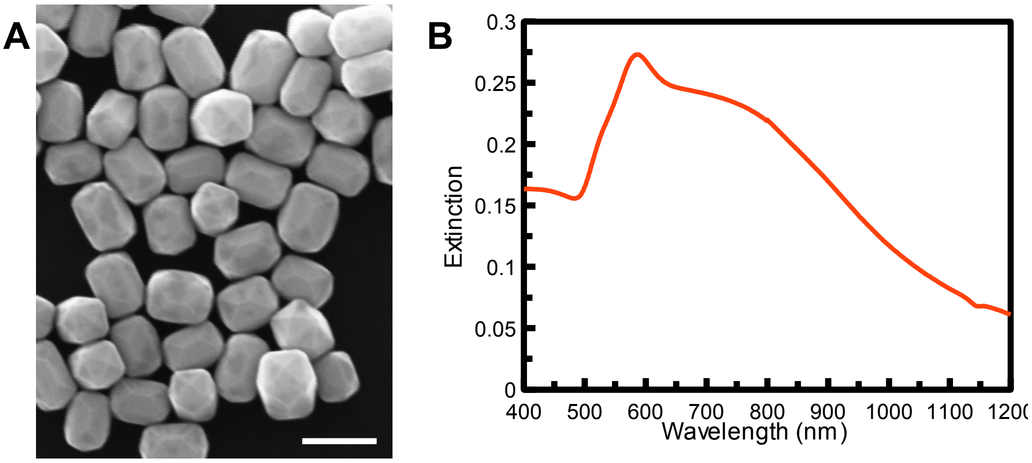

Figure 4.3: (A)Scanning electron microscope image of the gold nanorods with an average length and diameter of 190nm and 120nm, respectively. (B) Extinction spectrum of the gold nanorods in solution. Three resonances are visible in this spectrum: the longitudinal mode located around 760nm, the transversal mode around 570nm, and a quadrupolar mode around 600nm.

Regular rotation trapping experiments, as described in the previous paragraph, were conducted on 10 different nanoparticles to obtain the power dependences of the rotation frequencies and autocorrelation decay times for the gold nanorods in water against a glass interface. As seen in Figure 4.4, the similarities in the power dependences of the 10 different nanorod reflect the monodispersity of the colloidal suspension. The fittings from the autocorrelation functions to extract rotation frequency and autocorrelation decay time presented very good agreements as show the amplitudes of the error bars.

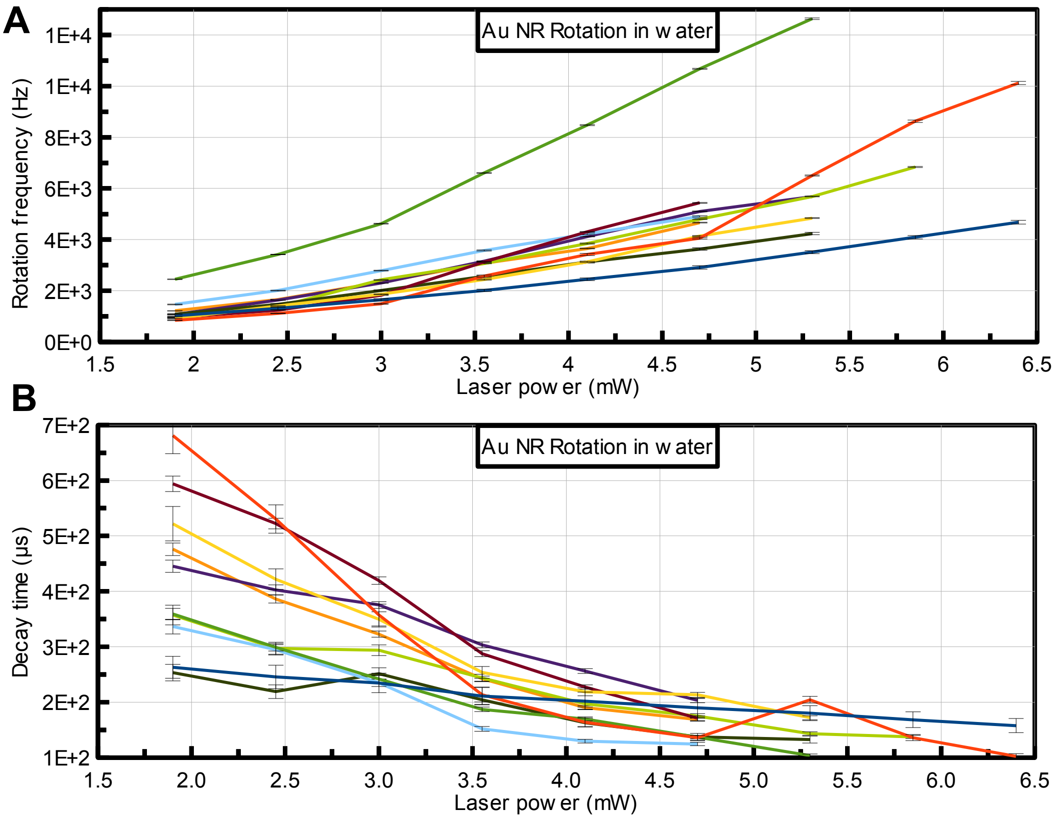

Figure 4.4: Gold nanorods trapped with a laser at 830nm in water against a glass interface. Power dependences of the rotation frequencies (A), and of the autocorrelation decay times (B).

Two different vegetable oils were selected to form our oil-water interfaces: soybean oil (Sigma-Aldrich), and triglyceride (Sigma-Aldrich). The reason for these two choices were the following. As of now, soybean oil volumes account for 25% of the world consumption in vegetable oil; only equalled by palmseed oil. This system is thus very relevant for applications in the industry. Triglyceride is a good oil reference since it is free of chemical surfactants that could cause unexpected phenomena. The aim of the experiment was to create a horizontal oil-water interface with the oil on top of the water. The water would contain the diluted solution of gold nanorods. Placing the sample in the optical tweezers, the gold nanorods would be slowly pushed upwards by moving the laser focus and be stopped by the oil due to its high viscosity. A 1.2µL droplet of oil is placed on what will become the top glass coverslip. After placing a 100µm-thick spacer on the bottom glass coverslip, a 2.8µL droplet of nanorods in solution is pipetted in its centre. After waiting some minutes for the oil to settle, the top glass coverslip is placed delicately so that the oil and water droplets coincide without escaping in the spacer matrix.

The horizontal oil-water interface position was visualized by observing the Brownian motion of particles in both media. Indeed water (η = 1.002mPa.s) has a much lower viscosity than soybean oil (η = 54.3mPa.s) and triglyceride (η = 60mPa.s). Brownian motion of particles are much faster in water. To have a statistically relevant amount of data, 10 gold nanorods were trapped both at soybean oil-water interface and triglyceride-water interface with a circularly polarized laser beam.

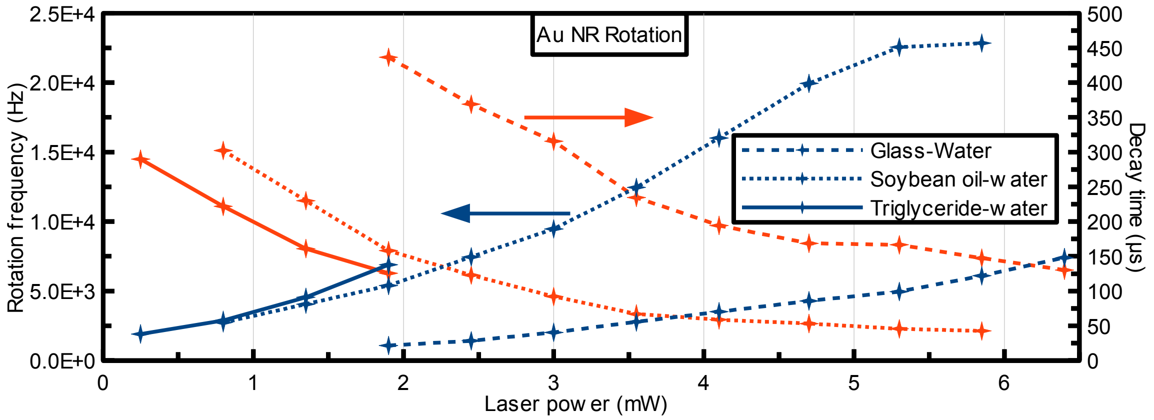

Figure 4.5: Au NR rotation frequencies (blue) and autocorrelation decay time (red) averages for a glass-water interface (dashed lines), soybean oil-water interface (dotted lines), and triglyceride-water interface (continuous lines)

To allow easier comparison, averages of the different power dependences are plotted in Figure 4.5. It is clear that rotation frequencies against the glass interface are around 3 times lower than at an oil-water interface. This result is coherent with the decay time values which are around 3 times higher for a glass-water interface. The problem lies in discovering the origin(s) of the decrease in apparent-viscosity at similar laser power when the nanoparticle is at an oil-water interface. Precise informations about the relative position of the nanorod with respect to each media during the rotation are not available. However, when released from the optical trap, the nanorod Brownian motion reveals that it is still located in water. Depending on the interface, the ranges of laser power available for a stable trap are different. The lowest power enabling trapping of a nanorod is reported for the triglyceride-water interface. On the other hand, nanorods are quickly lost in the oil phase for higher laser power.

It is known in classical hydrodynamics that the viscosity of a liquid in laminar flow increases when in vicinity to a wall. An hypothesis was that the water viscosity near glass (infinitely viscous) would be altered differently than near oil. A back-of-the-envelope calculation revealed that the water viscosity 5nm from the glass surface is only around 12% higher than 5nm away from the oil phase. Another factor that could modify the spin angular momentum transfer is the refractive index. But glass (n = 1.51) and triglyceride or soybean oil (n = 1.47) exhibit close values. An additional experiment was conducted to discover the orientation of nanorods during rotation. The dark-field spectra of rotating individual gold nanorods trapped with a laser at 660nm were measured at soybean oil-water interface and glass-water interface, and plotted in Figure 4.6. It is surprising to notice that the spectrum at the soybean oil-water interface looks like a single dipolar resonance positioned at the wavelength of the transversal mode. Compared to the broad spectrum at glass-water interface, it would point towards the fact that depending on the interface, the particle changes its orientation from being perpendicular to being parallel with respect to the light direction of propagation. On one hand it would explain the decrease in apparent-viscosity since rotation around its long axis would cause a lower drag. And indeed, for the same rotational frequency, the calculated friction torque using equation (4. 9) of a nanorod rotating horizontally is equal to 2.574 times the friction torque of a nanorod rotating vertically. On the other

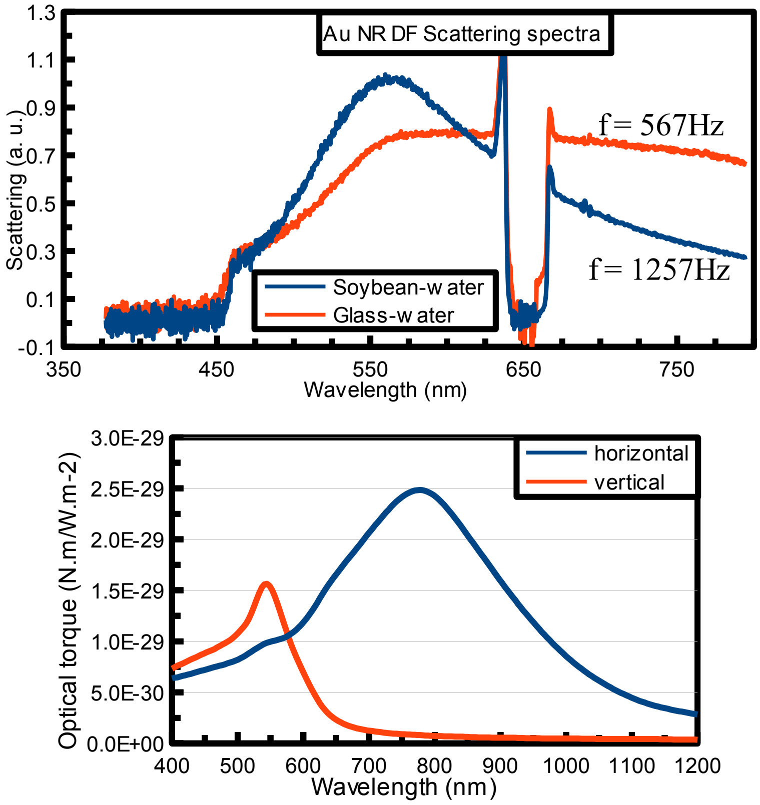

Figure 4.6: (Top)Dark-field scattering spectra of rotating nanorods trapped at 660nm with same laser power. (red)Nanorod trapped against glass and rotating at 567Hz. (blue)Nanorod trapped against soybean oil and rotating at 1257Hz. (Bottom)Calculated total optical torque on a horizontal (blue), and vertical (red) nanorod, respectively.

hand, the optical torque of the nanorod rotating vertically would decrease due to the position of the transversal resonance with respect to the laser line. The optical torque of a vertical and horizontal nanorod can be calculated from FDTD simulations (Figure 4.6). From these calculations, it would seem difficult for a completely vertical nanorod to have an optical torque able to induce a fast rotation. However, intermediate orientations would still have a considerable optical torque due to the broadband extinction spectrum of the nanorods. Chemical origins of the higher rotational frequency at oil-water interfaces are still left to be explored so far.

As a side effect of trapping at oil-water interface, I observed the formation of water-in-oil emulsion at the location of the trapped nanoparticle both for circularly polarized and linearly polarized laser beam. The increase in emulsion generation for linearly polarized light would indicate that heat is accelerating the emulsion since light absorption is more efficient for linearly than for circularly polarized light illumination at the same power. An increase in laser power resulted in an increase in emulsion generation. As said before, soybean oil contains surfactants such as diglycerides and fatty acids, which promote emulsion. Formation of water-in-oil droplets in a triglyceride-water system proved to be very difficult over the laser powers limited range without losing nanorods in the oil phase.

As a conclusion, water-in-oil emulsion generation seems to be linked to the presence of surfactants at the oil-water interface, and heat from the nanorods only acts as a secondary cause.

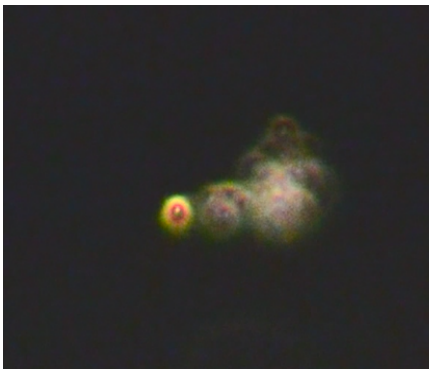

Figure 4.7: Dark field image of a rotating gold nanorod generating water-in-oil (soybean oil) emulsion for a laser power of 2.5mW. The cloud of droplets drifts in the oil phase. The droplets lifetime is of several seconds.

Chapter 5

Nanofabrication

Nanotechnology and nanofabrication go hand in hand. Driving further the possibilities of manufacturing more complex nanostructures and with higher precision allows to make progresses in fields like plasmonics. Generally, nanostructure production falls into two categories: bottom-up, and top-down. All the nanostructures presented in Papers II-IV were realized through hole-mask colloidal lithography.[48] One of the most common techniques to manufacture metallic nanostructures on substrate is through the use of a surface template. A good overview of different methods to fabricate plasmonic samples is given in a review by M. R. Jones *et al.*[153] The way it works is the following: a pattern is formed via different lithography techniques, material evaporation is used on the patterned template, and finally the template is removed to reveal the nanostructured film on a substrate. The most commonly employed methods in the literature are photolithography, which can produce quickly large patterned areas, and electron beam lithography, which has a high versatility and precision to manufacture templates. However, both these approaches are costly either in time or money. In comparison to electron beam lithography, colloidal lithography techniques are cheaper, quicker, facile, and can cover large areas. They can be used to produce ordered arrays with close-packed colloids templates.[154, 155] Hole-mask colloidal lithography (HCL) is processed similarly by adding a polymer-based sacrificial layer. HCL structures are typically short-range ordered owing to the charge repulsion between the colloids employed.[49] Density of nanostructures can be tuned by controlling the amount of charges in the colloidal beads solution. As I demonstrate more in detail in the following paragraphs, the colloids polydispersity is responsible for inhomogeneities in particle dimensions. Moreover, due to the spherical shape of the beads, nanoparticle features are limited. In conjunction with HCL, angular evaporation and rotating exposition are used in this thesis. It allows to overcome certain shape limitations and expand the range of designs available.

In this chapter, the first part is about the basics of hole-mask colloidal lithography. Then in a second part I look at some options that are important to consider during fabrication. In the third and last part of the chapter I discuss what kind of designs angular evaporation and simultaneous rotation open up to, as well as some of its limitations.

5. 1 Hole-mask colloidal lithography

HCL is a technique that has been used for many different structures, such as nanoholes,[156, 157], nanodisks,[158-160] dimers,[161] vertical dimers,[162, 163] oligomers,[164, 165] conical particles,[166] and rings or crescents.[167, 168] Figure 5.1 illustrates some of these examples fabricated in the MC2 cleanroom and imaged by scanning electron microscopy (SEM).

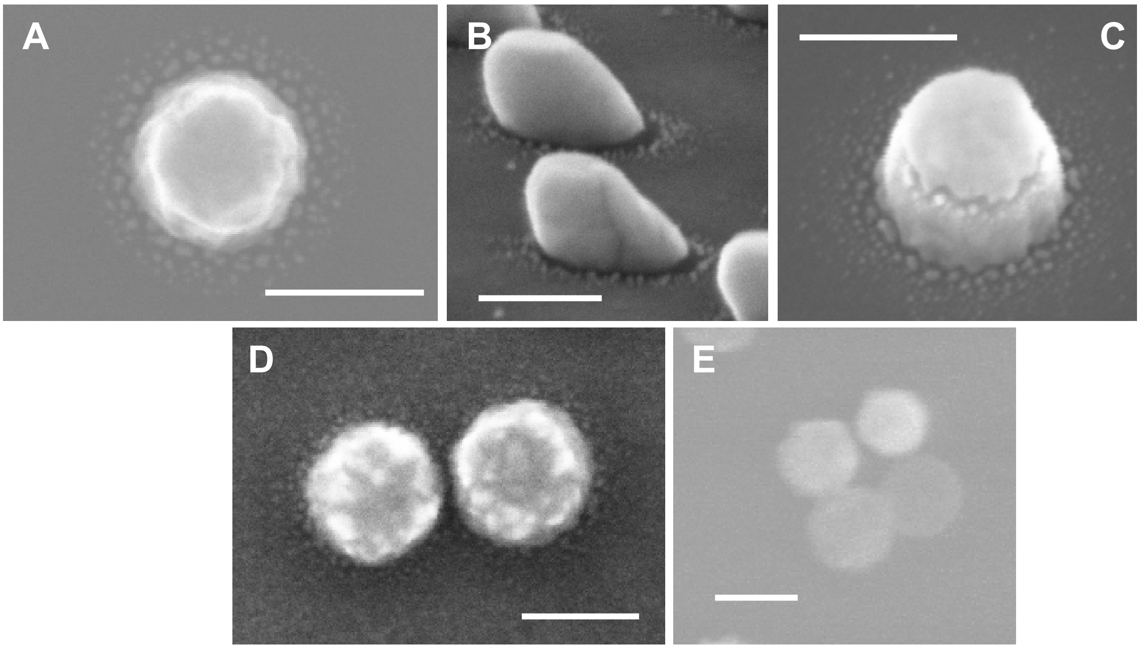

Figure 5.1: SEM images of diverse plasmonic nanostructures fabricated via HCL. (A) Gold nanodisk, (B) tilted gold monomer, (C) Au-SiO2-Au nanosandwich, (D) gold dimer, (E) gold tetramer. Scale bar = 100nm.

The two most basic structures fabricated by HCL are nanoholes and nanodisks. I go through the step-by-step recipe needed to achieve these two structures by following the schematic depicted in Figure 5.2.

1. As very often in sample preparation in a cleanroom, a clean sample is of great importance. To achieve that, the glass coverslip that serves as our substrate is first blown with a stream of nitrogen to remove the biggest dust particles. It is then followed by three successive ultrasonic baths (Acetone, Isopropanol, Deionized water) lasting 5 minutes each in a water at 50°C. Finally the sample is dried by a stream of nitrogen.
2. The glass is ready to be covered by a thin layer of PMMA (poly-methylmethacrylate), a light-sensitive polymer. This is done by first pipetting the diluted PMMA solution on top of the substrate, and by spin-coating to equalize the thickness over the sample. To finish the evaporation of the diluted PMMA, remaining solvent the sample is soft-baked either in an oven at 180°C for 10min or on a hot-plate for 5min. PMMA final thickness depends on multiple factors, such as the initial

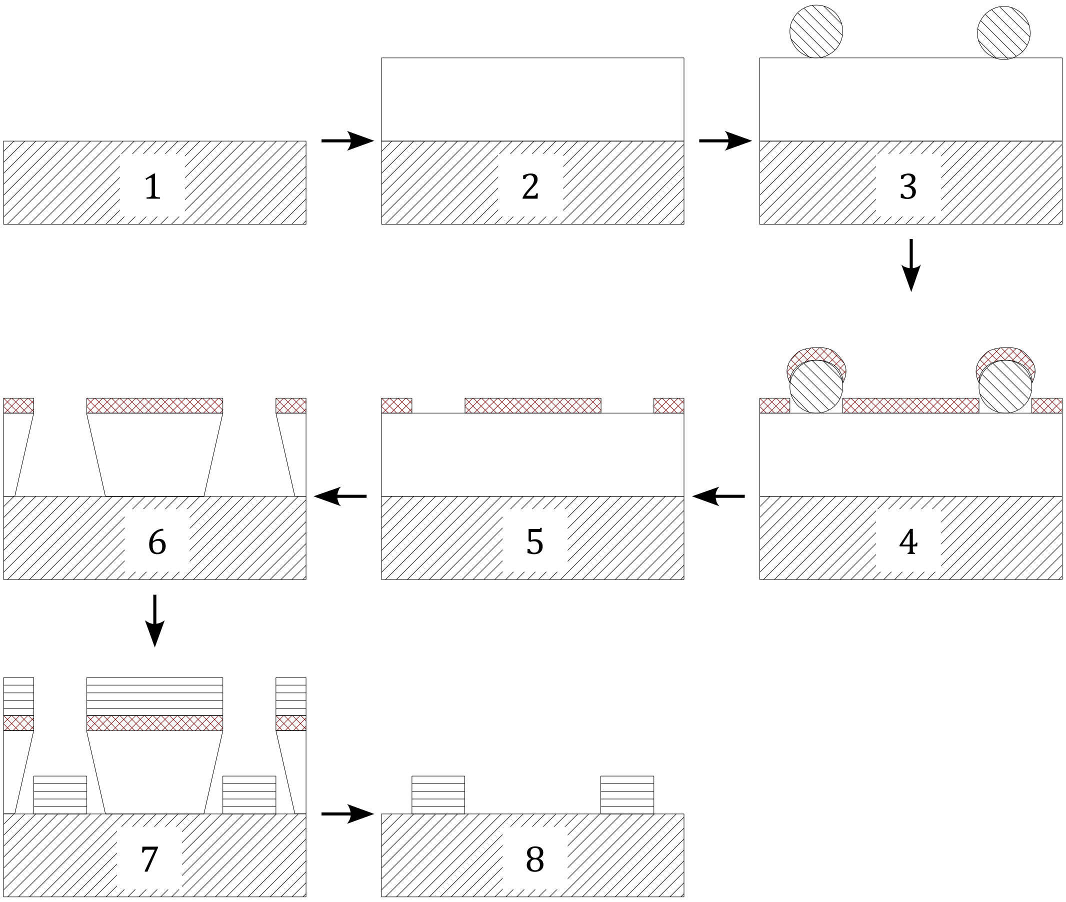

Figure 5.2: Step-by-step illustration of the HCL method to fabricate nanodisks on a substrate. The substrate is first cleaned, after which a polymer (PMMA) is spin-coated and soft-baked upon it. After a brief oxygen plasma etch, a monolayer of PDDA polyelectrolyte is coated on the surface. A solution of latex beads with opposite charges is then pipetted, rinsed, and the sample is dried. A metallic mask is deposited, the latex beads are tape-stripped away, and holes are pierced through PMMA by oxygen plasma etching. A second material evaporation at normal incidence deposits nanosdisks on the substrate. They are left free-standing after the lift-off step and some additional cleaning.

dilution, the time duration of the spinning, and the rotational speed of the spin-coating. Typically, these factors are chosen so that a resist layer thickness around 235nm (PMMA-A4, 4000rpm, 1min) is obtained.

3. Following the baking, a short (~5s, 50W) oxygen plasma etching step is required to induce hydrophilicity of the PMMA layer surface. Self-assembly of the latex beads in colloidal solution is realized by electrostatic attraction between the beads and the surface, and repulsion between the identically charged beads. To induce surface charges at the surface of the PMMA, a monolayer of a positively charged polyelectrolyte called PDDA (poly-diallyldimethylammonium) is deposited. This polyelectrolyte is spread on the polymer via pipetting a diluted solution (0,2% concentration), left to incubate a certain amount of time (30s), before being rinsed (10s) under a constant stream of deionized water. A stream of nitrogen to blow-dry the

sample substrate concludes the surface charging step. The negatively charged beads are found in suspension in aqueous solution whose concentration and charges content determine the density of the structures present on the substrate at the end of the recipe. This step is similar to the previous one. With a pipette, the solution of latex beads is spread on the sample surface and left incubating for a certain amount of time (1min), rinsed under a stream of deionized water (30s), and blow-dried under a stream of nitrogen. The final distribution of the beads layer is amorphous with a short-range order due to the repulsion forces between colloids. The purpose of rinsing and drying is to remove any excess beads still present and prevent any rearrangements of the "fixed" nanospheres.

4. The next step in the process is to evaporate a thin metallic film on top of our sample surface. This metal layer forms the mask template that is used during a future evaporation step, and removed during the lift-off step. Usually the metal deposited is either gold or chromium with a thickness of around 10nm. The only criterium this layer musts satisfy is that it has to be resistant to oxygen plasma etching.
5. After mask deposition, a tape-stripping process is used to remove the latex beads. After this step, what should be left is a mask perforated by circular holes where the beads were. A good adhesion between the tape and the sample surface is necessary to remove the beads. Alternatively, one can remove the beads by gently brushing the sample with a Q-tip.
6. A long (2-5min, 50W) oxygen plasma etching step etches away the PMMA not protected by the mask. It creates nanoholes which, with a proper timing of the etching, reaches the glass substrate surface. This timing depends both on the thickness of the PMMA one has to go through, and also on the undercut required for the particular process.
7. In this second material deposition, the desired structures are evaporated onto the substrate. Their shapes are dependent on the mask realized previously through steps 4 to 6. Their thickness depends on the evaporation duration and evaporation rate. Here, one can vary the materials evaporated to produce structures with different properties. In the example depicted in Figure 3.2, nanodisks, one only needs to do a single evaporation at normal incidence.
8. This step is the last in the recipe. Now that the structures are sitting on the surface of the substrate, one needs to remove all excess material on top of the PMMA layer as well as the PMMA itself so that they are left free-standing. It is simply done by repeating the cleaning from step 1. Acetone dissolves the PMMA, and all material resting on it is lifted away. The next ultrasonic baths completes the cleaning of the finished sample.

Despite the apparent simplicity of the HCL method, many choices are available at each step to tweak and tune the nanostructures pattern to your needs. Some considerations about the material evaporation method, annealing, and adhesion are developed more in detail in the next paragraph.

5. 2 Nanofabrication options

Material deposition

Different material deposition techniques have each their advantages and disadvantages with respect to the sample properties that are sought after. Physical vapour deposition (PVD) can be done via two main methods: evaporation, and plasma assisted sputtering. In sputtering, a material source also called target is bombarded by ions. The bombardment comes from a plasma localized close to the target by a magnet. The ions collides with the material source whose atoms are ejected away as a vapour in the deposition chamber. After an omnidirectional launch, this vapour condensates either on the chamber walls or on the substrate surface. The plasma gas is often an inert gas, such as argon. Changing the gas pressure changes the motion of the sputtered material vapour. The resulting deposition is a quite uniform coverage of both horizontal and vertical features due to the omnidirectionality of atom ejections. Deposition rate is generally higher than in the case of evaporation.

In the case of evaporation, the target is heated up to high temperatures up to the point where the material is evaporating. Heating is done either by resistive heating or by an electron-beam gun. Resistive heating is conducted by placing the material in a “boat” made from a temperature resistant material (Ta or W) and passing current through it. Alternatively, material can also be placed in a crucible and heated radiatively by an electric filament. On the other hand, an eletron-beam gun heats the material source directly by focusing a stream of electrons accelerated with voltages of several kilovolts onto the target. The electrons hit the source and their kinetic energy is transformed into thermal energy. The evaporation process takes place in high vacuum that can be achieved by a combination of a mechanical pump and a cryo-pump. High vacuum is needed so that once the material evaporates it can reach the sample surface and condensate. The evaporation rate is typically around 2Å/s and is directional. Coverage uniformity on the plane parallel to the target depends on the uniformity of the heating and on the distance from target to sample. Since the target has a limited size, the coverage right above it is thicker, and decreases as distance from it increases.

For both the evaporation technique and the sputtering technique a shutter separates source from sample until a stable deposition rate is reached for a more consistent material film. An advantage that evaporation has with respect with sputtering is its directionality. Indeed one can use a partial shutter to expose different parts of a deposition area with different thicknesses and/or materials.

Figure 5.3 is a good illustration of the differences in deposition between sputtering and evaporation. As I said before when explaining the HCL method, the mask layer is the template for the nanostructures. By evaporating at normal incidence, one ends up with nanodisks. Since the evaporation is directional, only few material satellites surround the nanoparticle. In step 6 of the HCL process, PMMA is etched and the etching time determines the size of the undercut at the PMMA-substrate interface. Since sputtering is omnidirectional, one can see that satellites have formed on the whole area available. The anisotropy of the satellites distribution is probably due to the positioning of the sample in the deposition chamber.

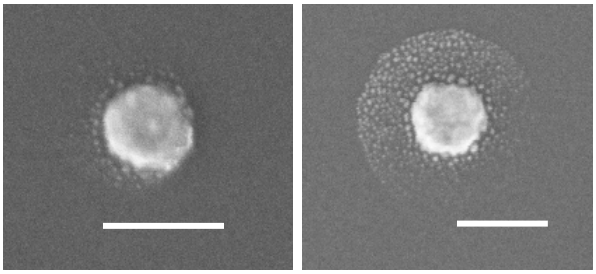

Figure 5.3: Gold nanodisks on Silicon substrate. (Left)An electron-beam gun was used to heat a gold target. (Right)An additional layer of gold (~10nm) was deposited by sputtering before lift-off. Scale bar = 100nm.

Annealing

Metal evaporation leads to a nanostructure consisting of many material grains. The higher the number of grain boundaries, the higher the losses. Annealing is a method to reduce the nanoparticles morphological aberrations. Simply put, heating up the sample after lift-off at at high temperature (above 200°C) for a short amount of time (~10min) causes grain coarsening in the nanostructure. The LSP resonance gains in intensity and decreases in bandwidth due to the gain in quality of the resonant modes. Associated with annealing, a reshaping effect can occur. Indeed, the particles try to minimize their surface energy by adopting a more spherical shape.[169] Thus an annealed particle becomes more "rounded" and its resonance blue-shifts. It can also be added that although annealing can enhance the plasmonic properties of a nanoparticle, sharp features might be lost in the process, such as depicted in Figure 5.4.

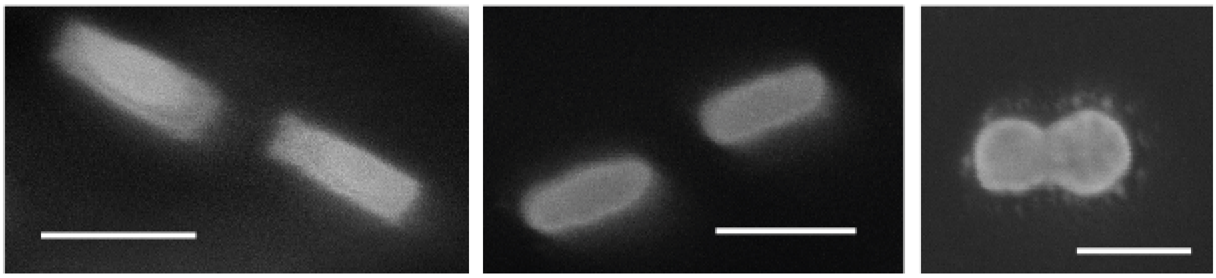

Figure 5.4: Elongated gold particles featured in Paper III. (Left)Before annealing the elongated particles have sharp corners. (Centre)After annealing, these same corners have disappeared. (Right)Gold dimer bridged by the annealing process. Scale bar = 100nm.

The reshaping effect can be used advantageously to quickly fabricate samples covered with small nanoparticles. By simply evaporating a thin layer (~10nm) of gold, for example, and then annealing, a surface of nanoparticles is formed from gold gathering into islands.[169] Annealing can be done on a hot-plate or in an oven for a better control of the environment. Indeed, heating some metal leads to a faster oxidation.

Adhesion layer

As its name suggests, an adhesion layer consists in evaporating a very thin film of metal (~1-3nm), such as chromium or titanium, prior to the evaporation of the main nanostructures to increase their adhesion to the substrate. In the case of annealing, the reshaping effect can be limited by this extra layer. Additional adhesion is necessary for thick nanoparticles that could otherwise get shaken up by an ultrasonic bath while cleaning. This can be a problem during the lift-off, but also in the framework of applications if the sample has to be re-used multiple times. Figure 5.5 illustrates what can happen during a cleaning step without an adhesion layer.

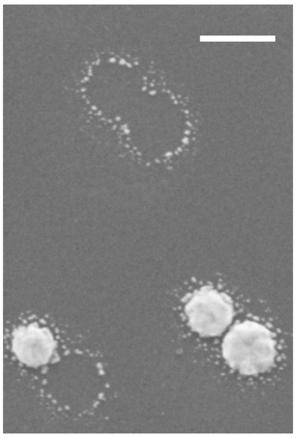

Figure 5.5: Gold dimers without adhesion layer on a silicon substrate. During the cleaning after lift-off, some of the 35nm-thick nanoparticles got loosen up leading to some incomplete and missing dimers. Scale bar = 100nm.

Aside from all these advantages, an adhesion layer also brings disadvantages. Chromium and titanium are metals with strong absorption. The LSPR resonance of a nanoparticle will be attenuated by it and its efficiency as a biosensor, for example, might be decreased.[170] The use of an adhesion layer has to be limited if possible.

5.3 Angular and rotating evaporation

Each degree of freedom available during the nanofabrication process expands greatly the number of designs available. Material evaporation is one of the steps that occurs the most often. One of the tools available in our cleanroom is a Lesker PVD225 evaporator. It has a 12-pockets barrel for different materials, e-gun evaporation, and operates at pressures below 10^{-7} Torr. The sample holder can tilt at an angle of ±45 degrees and can rotate in steps or continuously during evaporation. A simple schematic in Figure 5.6 represents the factors I am interested in in this paragraph. α represents the angle of the sample with respect to the normal, β is the partial opening angle of the intermediary fixed shutter between the sample and the source, and ω is the continuous jogging speed of the sample during evaporation. A basic use of continuous jogging speed is to obtain a uniform coverage when doing thin film deposition, and a partial fixed shutter allows to fabricate series of samples with different materials or parameter values without the need to unload the deposition chamber and pump again, thus gaining processing time.

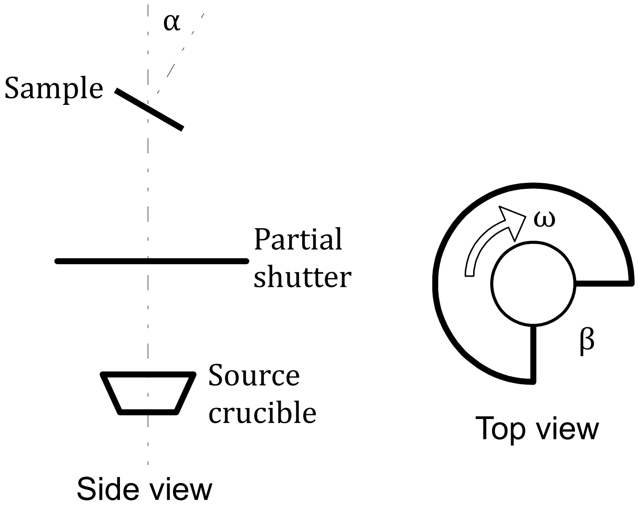

Figure 5.6: Schematic of the evaporator apparatus. Four different factors can be changed easily: the source material, the angle of evaporation α, the partial angular opening of a fixed shutter β, and the sample jogging speed ω.

Angular evaporation

Aside from these standard applications, one can explore different nanostructure designs.[161, 164-166] The first requirement is to have a large enough area at the PMMA-substrate interface to fit a nanostructure wider than a simple nanodisk. Proper timing of the plasma oxygen etching step is essential. If one wants to fabricate a tilted monomer such as in Figure 5.1, the only requirement is to evaporate at a certain angle α. The conical shape of the monomer comes from the fact that the mask circular aperture closes off as more and more material is evaporated.[164] Dimers fabrication is depicted in Figure 5.7A and is similar to fabricating two nanodisks, one after the other, at ±α. The angle α has to be chosen so that the two disks are not overlapping. A good estimation of α requires only to know the thickness of the resist layer and a bit of trigonometry.[164] Continuously evaporating while continuously changing the angle from +α to -α leads to the formation of elongated nanoparticles.

All of these nanostructures are possible by simply controlling the evaporation angle during the last evaporation step. Using angular evaporation to realize the mask is also known as shadow evaporation. When done correctly, instead or a circular aperture, an elliptical pattern appears in the mask as shown in Figure 5.7B. However, the produced ellipses have a rather limited aspect ratio (~2). For high angle of evaporation, the mask material that would be on top of the latex beads ends up being connected to the rest of the mask film. It then becomes impossible to remove the nanospheres by tape-stripping without tearing out parts of the mask.

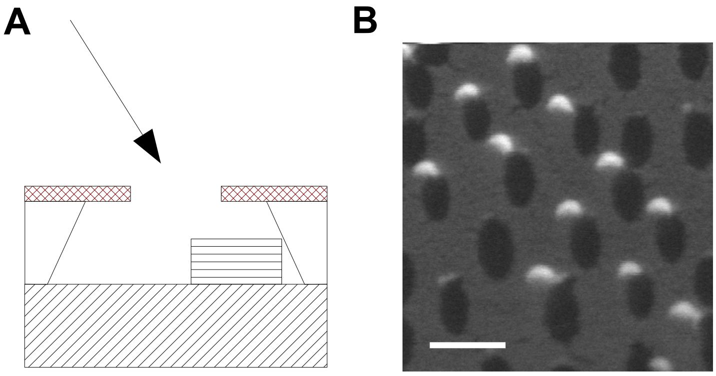

Figure 5.7: (A)Schematic of the evaporation at an angle +α of the first nanodisk that will constitute a dimer. (B)Mask evaporated by shadow evaporation but with only a partial removal of the latex beads.

Rotating Evaporation

Being able to rotate the sample holder enables to realize even more complex shapes, such as the tetramer in Figure 5.1. What needs to be kept in mind is that for whatever shape one intends to achieve, a single circular aperture in the mask is used. As more and more material is evaporated, the more this aperture shrinks. It can be used as an advantage,[164] or it can be a limitation.

Similarly to the method employed to fabricate dimers, tetramers are formed by the evaporation of four nanodisks one after the other at a fixed angle, with a rotation of the sample holder in between. Of course, this strategy is not limited to tetramers, it can be adapted for trimers, pentamers, etc. Moreover, as each element of the oligomer is evaporated independently from the others, different materials can be used as well as different thicknesses; the deposition angle can be modified, and the rotation angle can be controlled to achieve the design required. Based on angular and rotating evaporation, chiral spiral ramp nanostructures were reported in the literature.[171] Coupling a continuous rotation of the sample holder with angular deposition would only result in a crescent-like nanoparticle. To realize a ramp, two solutions are possible. One solution is to have a slow decrease in the rotational speed to accumulate material. The second solution is to have a constant rotational speed but an increasing evaporation rate.

So far I didn't use the possibility of including a partial shutter between the source target and the sample. Nonetheless it can be a very powerful tool in the processing of metasurfaces. A partial shutter will only allow a fraction of the sample to be exposed. By aligning the sample position on the holder with its centre of rotation, continuous rotation during the deposition step leads to a metasurface with a rotational symmetry. Rotational symmetry on a metasurface based on HCL holds some potential in the nanofabrication of polarizers that are so far restricted to electron-beam lithography.[172-174]

One of the great strengths of HCL is its capability to cover large areas very easily in a uniform manner as shown in Figure 5.8. Covering several square centimetres using electron-beam lithography would take much more processing time. One can leverage the large coverage advantage of HCL thanks to a partial shutter. A comprehensive overview

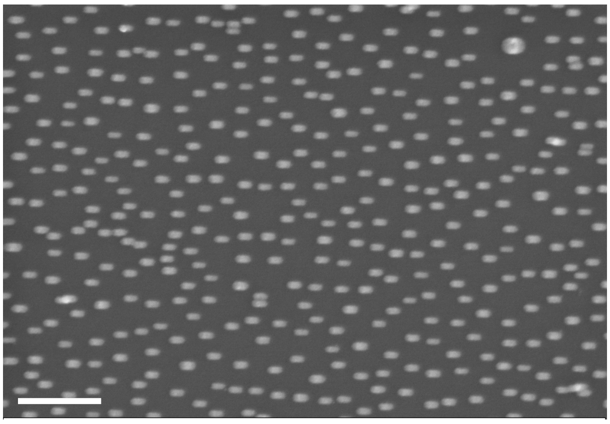

Figure 5.8: Elongated gold nanoparticles on a silicon substrate. Scale bar = 1µm.

of the combinations made possible by the use of a partial shutter, angular evaporation, and rotation of the sample can be found in Paper IV. Let's consider the deposition at normal incidence of a film on a substrate. Let's also insert a partial shutter with an angular opening β = 90° and rotate the sample at a constant speed. During the continuous rotation, there is a constant accumulation of material over the 90° arc exposed. This will create a thickness gradient with a polar distribution. The gradient can be controlled by the rotational speed for a fixed evaporation rate. Because of the very slow deposition rate (2Å/s), a very high precision can be realized. It means that the thickness parameter can be varied continuously over the sample surface. This is especially useful in the case of optimization. What is finally realized is a "library" of nanostructures on a single sample in a single evaporation step. Not only that, but a thickness gradient in the mask template results in a lateral gradient when fabricating dimers for example. However, the mask thickness gradient presents two limitations. The maximum thickness cannot be higher than the radius of the latex beads, otherwise tape-stripping would be rendered impossible. The second limitation concerns the material used as a mask. As the mask becomes thicker, the material capping the beads not only grows in thickness but also in lateral dimensions. To limit this lateral growth, a material with a small grain size, such as chromium is preferred.

Chapter 6

Summary and Outlook

Summary of Appended Papers

Paper I: *Ultrafast Spinning of Gold Nanoparticles in Water Using Circularly Polarized Light* is a report about the rotation of gold colloids trapped in water in two-dimensions by near-infrared laser tweezers. The transfer of spin angular momentum from circularly polarized light to the nanoparticle induces rotation at frequencies of several kilohertz. At the time of the publication, it was the first time that such high spinning frequencies were reached in water. What the paper puts in evidence is the relationship between the aborption cross-section of the particles and the transfer of spin angular momentum. A clear increase in the spinning frequency is observable when the laser power is increased. Tracking of the nanoparticles rotation is possible thanks to intensity correlation measurements. The imperfections in the shape of the gold colloids creates small variations in the collected light intensities. The analysis of the APD data gives an autocorrelation function showing two features that are attributed to two phenomena: the oscillation of the autocorrelation function corresponds to the rotation of the nanoparticle, the autocorrelation function decay time is associated to the rotational Brownian motion. The autocorrelation decay time is a function of viscosity, temperature, and rotation frequency of the nanoparticle. An observation of the decrease of this decay time with respect to an increase of the laser power points to the fact that an increase in temperature in the vicinity of the trapped particle is decreasing the local viscosity.

Paper II: *Macroscopic Layers of Chiral Plasmonic Nanoparticle Oligomers from Colloidal Lithography* is a study of artificial chiral plasmonic structures composed of three to four nanodisks. The nanofabrication of the chiral nanostructures is based on the hole-mask colloidal lithography method and on angular metallic evaporation. A very strong chiral optical activity is observed in these oligomers in the visible to near-infrared wavelength range. The optical activity is evaluated by a quantity commonly used in biology and chemistry called circular dichroism. Circular dichroism is a measurement of the difference in light intensities when the sample is illuminated by RCP and LCP light. A maximum difference of 7% between the two light handedness is measured in transmission for silver tetramers. To understand the origins of the optical activity in tetramers (fabricated as four disks of increasing heights on a square base), simulations were conducted with two methods (CDA and FEM) and compared. CDA is a simplified model whose limitations put forward some interaction contributions when placed side-to-side with the more complete system simulated via FEM. From our analysis, the tetramers optical activity is dominated at longer wavelengths by the interactions between the two dipolar resonances from the two thinner disks. At shorter wavelengths, contributions are coming from quadrupolar modes and dipolar modes from the two taller disks. Near-field coupling between the disks is a crucial point underestimated in the CDA. Symmetry-breaking of the structure is another requirement to have an optically active structure. The potential of tetramers for enantiomer sensing can be evaluated by the observation of the superchiral fields of the nanostructure. To conclude, despite high local values, the average value over the whole nanostructure is not very promising. The circular dichroism of the tetramer structure itself would dominate the overall signal.

Paper III: *Near-Complete Photon Spin Selectivity in a Metasurface of Anisotropic Plasmonic Antennas* presents the design of a metasurface able to select the circularly polarized light reflected. A metasurface composed by a dense array of elongated gold nanoparticles is fabricated based on hole-mask colloidal lithography. The idea is to use an evanescent illumination scheme which results in an orientation of the electric field in the sample plane along two different directions depending on the impinging light handedness. By orienting the elongated particles and aligning them along one of these two directions, the anisotropic nanoparticles are excited by either right- or left-handed circularly polarized light. A spin-selectivity of 90.4% is achieved this way. The system composed of the anisotropic nanoparticles and the oblique light illumination defines the so-called extrinsic chirality. The advantages of such systems is the ability to access both structure eniantomeric forms from the same sample, and the ease in the fabrication of the sample compared with intrinsic chiral nanostructures. The use of the modified Fresnel coefficients are perfectly able to model experimental results. The polarization state of the reflected light maintains a large degree of circular polarization under most polarization states of the illumination and shows an interesting singularity-like switching behavior for certain illumination conditions.

Paper IV: *Continuous Gradient Plasmonic Nanostructures Fabricated by Evaporation on a Partially Exposed Rotating Substrate* is the description of a nanofabrication technique based on hole-mask colloidal lithography. The aim is to leverage the ability of hole-mask colloidal lithography to fabricate quickly large areas for the realization of a “library” of nanoparticles on a single substrate. The possibility to continuously vary a parameter should prove invaluable in the optimization of nanostructures optical properties. Optical properties of nanostructures can be predicted by simulation, but it cannot take into account all of the non-ideal cases encountered in fabrication, or the irreproducibility of some experimental conditions. The basic principle relies on evaporation on a partially exposed rotating substrate. A fixed partial shutter only exposes a part of the substrate to the evaporated material. As the substrate rotates, the area exposed accumulates material. This results in a film with a thickness gradient with a polar topology. This variant on evaporation can be used at different stages of the HCL method for different purposes such as nanodisks with continuously varying thicknesses, sandwich structures with a gradient in the spacer thickness, nanoparticle dimers with continuously increasing gap distances, and crescent-like nanoparticles with continuously changing orientations.

Outlook

As one can read in this thesis, circularly polarized light interacts in many interesting ways with surface plasmons. Chiral nanostructures can be used for various applications such as polarizers, enantioselective biosensors, negative refractive index metamaterials, etc. Optical tweezers and transfer of angular momentum lead to unprecedented plasmonic nanoparticle rotation frequencies, and intriguing behaviours are observed at oil-water interfaces. Nanofabrication limits of hole-mask colloidal lithography are pushed further. However interesting opportunities are still left unexplored.

Combining nanofabrication and optical forces, plasmonic optical tweezers offer great prospects for the direct manipulation of single molecules. Using plasmonic dipole antennas, particles 10nm in size can be trapped in parallel.[122] An issue always present in the field of optical trapping is the heat-induced convection from light absorption in the metals. In plasmonic optical tweezing, a large area is illuminated to create several trapping spots observed simultaneously. However, it doesn't mean that a high density of antennas are needed to trap a few particles. The antennas can be tailored to the particle size required and can provide on-demand SERS hotspots for instance. A more interesting application of plasmonic optical tweezers is the transfer of angular momentum. Rotating nanoparticles can serve as mixers in microfludic systems, or micro-rheology probes. Two-dimensional chiral structure have already been used for the selective trapping of particles depending on the handedness of the incoming light.[175] However, the self-spinning of a nanoparticle by a plasmon-enhanced optical tweezers has not been achieved. With the new possibilities now offered by hole-mask colloidal lithography, the development of chiral plasmonic optical tweezers might be possible.

Enantiomer-sensing is a more difficult subject. Superchiral fields are seen as a way to enhance molecular chiroptical effects. However, most of the nanostructures showing strong optical activity are not suitable for enantiomer sensing as their own circular dichroism risks to dominate the molecular signature. As we observed in Paper II and III, superchiral fields can present a high local enhancement. But what matters is the average of superchiral field enhancement over the whole nanostructure since the sensing occurs by covering with chiral molecules the whole sample. There are at least two alternatives. One is the realization of a uniform superchiral field to avoid the averaging of positive and negative superchiral fields. The second is to have a very selective delivery of the analyte at a superchiral “hotspot”. Optical forces could be used, as well a combination of nanofabrication and surface chemistry.

But in the immediate future, investigation of optical trappping at oil-water interfaces is the priority. It proposes intriguing possibilities as a new tool to mechanically probe interfaces relevant to a major sector of the industry, and as a nanoscale source of emulsion. First of all, the origins of the observed increase in rotation frequency are left to be determined. The orientation change of the nanorod depending on the interface and the high sensitivity of the rotation frequency associated could prove useful in biological applications including lipid bilayers for example.

In conclusion, light polarization manipulation by single nanoparticles and metasurfaces is a subject with a lot left to investigate. Combining the two is not such a far-fetched idea and research is made in that direction to unlock its potential.

Acknowledgements

First of all, I would like to thank my supervisor, Mikael Käll, for all the patience he displayed, for all the work opportunities he provided, and for all the support with our articles. I am grateful to have been given the chance to work in the BNP group with all these talented individuals. Thanks as well for giving me the freedom to try things on my own. I would also like to thank my co-supervisor Peter Johansson for his assistance in the more fundamental aspects of plasmonics and the help in articles.

I wish to thank all my co-authors without whom publishing these articles would simply have not been possible. Thank you Anni for your hard work in the project we shared. Thank you Yurui for all the simulations you had to repeat again and again. Thank you Mikael S. for all the lengthy calculations, measurements, and writing that I forced you to do. Thank you Lei for your patience, work, and our discussions about our common paper. Thanks to Validimir, Si, Zhaleh, Kristof, Lei and Ruggero for all the help in the cleanroom.

Over 5 years, the members of the BNP group changed a lot. We expanded, contracted, hosted guests, changed floors and evolved overall. Thank you to the old, new, and temporary members of the BNP group for the great working environment.

Thanks again to Si and Yurui for sharing an office with me these last years. Thanks to Vlada, Kristof, Mikael S., Anni, and Gülis, for the places we explored together. May you continue roaming the world. Thank you Kristof for the beers we shared. I know you will drink a lot more. Thanks to Ruggero, Mohktar and Virginia for the impromptu picnics in parks and gardens. Thank you Yurui, Lei, Kunli, Yang, and Zhong-Jian for all the dinners you invited me to. Thank you Andreas and Gustav for playing boardgames and letting me win. Thank you Aron and Inès for the drinks and games at the pub. Thank you Ruggero and Nils for the good moments at the bars we went sitting at. Thanks to Timur for the discussions and your enthusiasm about science. Thank you Gustav E. for sharing the long teaching hours on many Thursdays. Thanks to everybody for sitting and sharing cakes among other things on Fridays, Kristoffer, Srdjan, Tomasz, Martin, Faegheh, Daniel, Hana, and the magnetoplasmonics crew.

Thanks a lot to Michelle who has shared her life with me during the last three years (and hopefully will share for longer).

Finally, many thanks to my family who has always supported me through all my decisions and despite the distance. Let´s see where is the next part of the journey.

Bibliography

[1] Kelvin, W. T. *Baltimore Lectures on Molecular Dynamics and the Wave Theory of Light*; Cambridge University Press,2010, 1904.

[2] Le Bel, J. A. Sur Les Relations Qui Existent Entre Les Formules Atomiques Des Corps Organiques et Le Pouvoir Rotatoire de Leurs Dissolutions. *Bull. la Société Chim.* **1874**, *22*.

[3] van't Hoff, J. H. Sur Les Formules de Structures Dans L'espace. *Arch. Néerlandaises des Sci. Exactes Nat.* **1874**, *9*.

[4] Faraday, M. The Bakerian Lecture: Experimental Relations of Gold (and Other Metals) to Light. *Philos. Trans. R. Soc. London* **1857**, *147*, 145–181.

[5] Mie, G. Beiträge Zur Optik Trüber Medien, Speziell Kolloidaler Metallösungen. *Ann. Phys.* **1908**, *330*, 377–445.

[6] Hendry, E.; Mikhaylovskiy, R. V; Barron, L. D.; Kadodwala, M.; Davis, T. J. Chiral Electromagnetic Fields Generated by Arrays of Nanoslits. *Nano Lett.* **2012**, *12*, 3640–3644.

[7] Hentschel, M.; Wu, L.; Schäferling, M.; Bai, P.; Li, E. P.; Giessen, H. Optical Properties of Chiral Three-Dimensional Plasmonic Oligomers at the Onset of Charge-Transfer Plasmons. *ACS Nano* **2012**, *6*, 10355–10365.

[8] Kuzyk, A.; Schreiber, R.; Fan, Z.; Pardatscher, G.; Roller, E.-M.; Högele, A.; Simmel, F. C.; Govorov, A. O.; Liedl, T. DNA-Based Self-Assembly of Chiral Plasmonic Nanostructures with Tailored Optical Response. *Nature* **2012**, *483*, 311–314.

[9] Gansel, J. K.; Thiel, M.; Rill, M. S.; Decker, M.; Bade, K.; Saile, V.; von Freymann, G.; Linden, S.; Wegener, M. Gold Helix Photonic Metamaterial as Broadband Circular Polarizer. *Science* **2009**, *325*, 1513–1515.

[10] Meinzer, N.; Hendry, E.; Barnes, W. L. Probing the Chiral Nature of Electromagnetic Fields Surrounding Plasmonic Nanostructures. *Phys. Rev. B* **2013**, *88*, 041407.

[11] Lu, F.; Tian, Y.; Liu, M.; Su, D.; Zhang, H.; Govorov, A. O.; Gang, O. Discrete Nanocubes as Plasmonic Reporters of Molecular Chirality. *Nano Lett.* **2013**, *13*, 3145–3151.

[12] Li, W.; Coppens, Z. J.; Besteiro, L. V; Wang, W.; Govorov, A. O.; Valentine, J. Circularly Polarized Light Detection with Hot Electrons in Chiral Plasmonic Metamaterials. *Nat. Commun.* **2015**, *6*, 8379.

[13] Kepler, J. *De Cometis Libelli Tres*; Andrea Apergeri: Augsburg, 1619.

[14] Ashkin, A.; Dziedzic, J. M.; Bjorkholm, J. E.; Chu, S. Observation of a Single-Beam Gradient Force Optical Trap for Dielectric Particles. *Opt. Lett.* **1986**, *11*, 288–290.

[15] Neuman, K. C.; Nagy, A. Single-Molecule Force Spectroscopy: Optical Tweezers, Magnetic Tweezers and Atomic Force Microscopy. *Nat. Methods* **2008**, *5*, 491–505.

[16] Wang, M. D.; Yin, H.; Landick, R.; Gelles, J.; Block, S. M. Stretching DNA with Optical Tweezers. *Biophys. J.* **1997**, *72*, 1335–1346.

[17] Svoboda, K.; Block, S. M. Optical Trapping of Metallic Rayleigh Particles. *Opt. Lett.* **1994**, *19*, 930.

[18] Anger, P.; Bharadwaj, P.; Novotny, L. Enhancement and Quenching of Single-Molecule Fluorescence. *Phys. Rev. Lett.* **2006**, *96*, 113002.

[19] Kühn, S.; Håkanson, U.; Rogobete, L.; Sandoghdar, V. Enhancement of Single-Molecule Fluorescence Using a Gold Nanoparticle as an Optical Nanoantenna. *Phys. Rev. Lett.* **2006**, *97*, 017402.

[20] Wessel, J. Surface-Enhanced Optical Microscopy. *J. Opt. Soc. Am. B* **1985**, *2*, 1538.

[21] Kelly, K. L.; Coronado, E.; Zhao, L. L.; Schatz, G. C. The Optical Properties of Metal Nanoparticles: The Influence of Size, Shape, and Dielectric Environment. *J. Phys. Chem. B* **2003**, *107*, 668–677.

[22] Prodan, E.; Nordlander, P. Plasmon Hybridization in Spherical Nanoparticles. *J. Chem. Phys.* **2004**, *120*, 5444–5454.

[23] Nordlander, P.; Oubre, C.; Prodan, E.; Li, K.; Stockman, M. I. Plasmon Hybridization in Nanoparticle Dimers. *Nano Lett.* **2004**, *4*, 899–903.

[24] Maxwell Garnett, J. C. Some Aspects of Mass Spectrometry in Research on Steroids. *Philos. Trans. R. Soc. A Math. Phys. Eng. Sci.* **1904**, *203*, 385–420.

[25] Myroshnychenko, V.; Rodríguez-Fernández, J.; Pastoriza-Santos, I.; Funston, A. M.; Novo, C.; Mulvaney, P.; Liz-Marzán, L. M.; García de Abajo, F. J. Modelling the Optical Response of Gold Nanoparticles. *Chem. Soc. Rev.* **2008**, *37*, 1792.

[26] Jackson, J. D. *Classical Electrodynamics, 3rd Ed.*; John Wiley & Sons, 1999.

[27] Wood, R. W. On a Remarkable Case of Uneven Distribution of Light in a Diffraction Grating Spectrum. *Proc. Phys. Soc. London* **1902**, *18*, 269–275.

[28] Wood, R. Diffraction Gratings with Controlled Groove Form and Abnormal Distribution of Lntensity. *Philos. Mag. Ser. 6* **1912**, *23*, 310–317.

[29] Yeh, P. *Optical Waves in Layered Media*; Wiley, 1988.

[30] Pines, D.; Bohm, D. Collective Description of Electron Interactions. *Phys. Rev.* **1952**, *85*, 338–353.

[31] Pines, D. Collective Energy Losses in Solids. *Rev. Mod. Phys.* **1956**, *28*, 184–198.

[32] Drude, P. *Lehrbuch Der Optik*; Hirzel: Leipzig, 1900.

[33] Homola, J. Surface Plasmon Resonance Sensors for Detection of Chemical and Biological Species. *Chem. Rev.* **2008**, *108*, 462–493.

[34] Ritchie, R. H.; Eldridge, H. B. Optical Emission from Irradiated Foils. I. *Phys. Rev.* **1962**, *126*, 1935–1947.

[35] Teng, Y.-Y.; Stern, E. A. Plasma Radiation from Metal Grating Surfaces. *Phys. Rev. Lett.* **1967**, *19*, 511–514.

[36] Kretschmann, E.; Raether, H. Radiative Decay of Non-Radiative Surface Plasmons Excited by Light. *Z. Naturforsch.* **1968**, *23*, 2135–2136.

[37] Otto, A. Excitation of Nonradiative Surface Plasma Waves in Silver by the Method of Frustrated Total Reflection. *Zeitschrift für Phys.* **1968**, *216*, 398–410.

[38] Svedendahl, M.; Chen, S.; Dmitriev, A.; Käll, M. Refractometric Sensing Using Propagating versus Localized Surface Plasmons: A Direct Comparison. *Nano Lett.* **2009**, *9*, 4428–4433.

[39] Bohren, C. F.; Huffman, D. R. *Absorption and Scattering of Light by Small Particles*; Wiley-VCH Verlag GmbH: Weinheim, Germany, 1998.

[40] Kreibig, U.; Vollmer, M. *Optical Properties of Metal Clusters*; Springer Series in Materials Science; Springer Berlin Heidelberg: Berlin, Heidelberg, 1995; Vol. 25.

[41] Anker, J. N.; Hall, W. P.; Lyandres, O.; Shah, N. C.; Zhao, J.; Van Duyne, R. P. Biosensing with Plasmonic Nanosensors. *Nat. Mater.* **2008**, *7*, 442–453.

[42] Link, S.; Mohamed, M. B.; El-Sayed, M. A. Simulation of the Optical Absorption Spectra of Gold Nanorods as a Function of Their Aspect Ratio and the Effect of the Medium Dielectric Constant. *J. Phys. Chem. B* **1999**, *103*, 3073–3077.

[43] Meier, M.; Wokaun, A. Enhanced Fields on Large Metal Particles: Dynamic Depolarization. *Opt. Lett.* **1983**, *8*, 581.

[44] Draine, B. T.; Flatau, P. J. Discrete-Dipole Approximation For Scattering Calculations. *J. Opt. Soc. Am. A* **1994**, *11*, 1491.

[45] Jensen, T.; Kelly, L.; Lazarides, A.; Schatz, G. C. Electrodynamics of Noble Metal Nanoparticles and Nanoparticle Clusters. *J. Clust. Sci.* **1999**, *10*, 295–317.

[46] Zhao, L.; Kelly, K. L.; Schatz, G. C. The Extinction Spectra of Silver Nanoparticle Arrays: Influence of Array Structure on Plasmon Resonance Wavelength and Width. *J. Phys. Chem. B* **2003**, *107*, 7343–7350.

[47] Markel, V. A.; Shalaev, V. M.; Stechel, E. B.; Kim, W.; Armstrong, R. L. Small-Particle Composites. I. Linear Optical Properties. *Phys. Rev. B* **1996**, *53*, 2425–2436.

[48] Fredriksson, H.; Alaverdyan, Y.; Dmitriev, A.; Langhammer, C.; Sutherland, D. S.; Zäch, M.; Kasemo, B. Hole–Mask Colloidal Lithography. *Adv. Mater.* **2007**, *19*, 4297–4302.

[49] Hanarp, P.; Käll, M.; Sutherland, D. S. Optical Properties of Short Range Ordered Arrays of Nanometer Gold Disks Prepared by Colloidal Lithography. *J. Phys. Chem. B* **2003**, *107*, 5768–5772.

[50] Bedeaux, D.; Vlieger, J. *Optical Properties of Surfaces*; Imperial College Press: London, 2001.

[51] Thongrattanasiri, S.; Koppens, F. H. L.; García de Abajo, F. J. Complete Optical Absorption in Periodically Patterned Graphene. *Phys. Rev. Lett.* **2012**, *108*, 047401.

[52] Svedendahl, M.; Käll, M. Fano Interference between Localized Plasmons and Interface Reflections. *ACS Nano* **2012**, *6*, 7533–7539.

[53] Arago, D. F. J. *Mémoire Sur Une Modification Remarquable Qu'éprouvent Les Rayons Lumineux Dans Leur Passage à Travers Certains Corps Diaphanes, et Sur Quelques Autres Nouveaux Phénomènes D'optique*; Didot, F., Ed.; Institut Impérial de France: Paris, 1811; Vol. 1.

[54] Biot, J.-B. *Mémoire Sur de Nouveaux Rapports Qui Existent Entre La Réflexion et La Polarisation de La Lumière Par Les Corps Cristallisés*; Didot, F., Ed.; Institut Impérial de France, 1812.

[55] Fresnel, M. A. *Mémoire Sur La Double Refraction*; Académie des Sciences, 1822.

[56] Pasteur, L. *Mémoire Sur La Relation Qui Peut Exister Entr La Forme Cristalline et La Composition Chimique, et Sur La Cause de La Polarization Rotatoire*; Académie des Sciences, 1848.

[57] Cotton, A. Absorption Inégale Des Rayons Circulaires Droit et Gauche Dans Certains Corps Actifs. *Comptes rendus* **1895**, *120*.

[58] Giloan, M.; Astilean, S. Negative Index Optical Chiral Metamaterial Based on Asymmetric Hexagonal Arrays of Metallic Triangular Nanoprisms. *Opt. Commun.* **2014**, *315*, 122–129.

[59] Kanda, N.; Konishi, K.; Kuwata-Gonokami, M. Terahertz Wave Polarization Rotation with Double Layered Metal Grating of Complimentary Chiral Patterns. *Opt. Express* **2007**, *15*, 11117.

[60] Kuwata-Gonokami, M.; Saito, N.; Ino, Y.; Kauranen, M.; Jefimovs, K.; Vallius, T.; Turunen, J.; Svirko, Y. Giant Optical Activity in Quasi-Two-Dimensional Planar Nanostructures. *Phys. Rev. Lett.* **2005**, *95*, 227401.

[61] Zhao, Y.; Belkin, M. A.; Alù, A. Twisted Optical Metamaterials for Planarized Ultrathin Broadband Circular Polarizers. *Nat. Commun.* **2012**, *3*, 870.

[62] Hendry, E.; Carpy, T.; Johnston, J.; Popland, M.; Mikhaylovskiy, R. V; Lapthorn, A. J.; Kelly, S. M.; Barron, L. D.; Gadegaard, N.; Kadodwala, M. Ultrasensitive Detection and Characterization of Biomolecules Using Superchiral Fields. *Nat. Nanotechnol.* **2010**, *5*, 783–787.

[63] Fedotov, V. A.; Mladyonov, P. L.; Prosvirnin, S. L.; Rogacheva, A. V; Chen, Y.; Zheludev, N. I. Asymmetric Propagation of Electromagnetic Waves through a Planar Chiral Structure. *Phys. Rev. Lett.* **2006**, *97*, 167401.

[64] Liu, M.; Zentgraf, T.; Liu, Y.; Bartal, G.; Zhang, X. Light-Driven Nanoscale Plasmonic Motors. *Nat. Nanotechnol.* **2010**, *5*, 570–573.

[65] Schwanecke, A. S.; Krasavin, A.; Bagnall, D. M.; Potts, A.; Zayats, A. V; Zheludev, N. I. Broken Time Reversal of Light Interaction with Planar Chiral Nanostructures. *Phys. Rev. Lett.* **2003**, *91*, 247404.

[66] Papakostas, A.; Potts, A.; Bagnall, D. M.; Prosvirnin, S. L.; Coles, H. J.; Zheludev, N. I. Optical Manifestations of Planar Chirality. *Phys. Rev. Lett.* **2003**, *90*, 107404.

[67] Vallius, T.; Jefimovs, K.; Turunen, J.; Vahimaa, P.; Svirko, Y. Optical Activity in Subwavelength-Period Arrays of Chiral Metallic Particles. *Appl. Phys. Lett.* **2003**, *83*, 234.

[68] Drezet, A.; Genet, C.; Laluet, J.; Ebbesen, T. W. Optical Chirality without Optical Activity: How Surface Plasmons Give a Twist to Light. *Opt. Express* **2008**, *16*, 12559.

[69] Fan, Z.; Govorov, A. O. Plasmonic Circular Dichroism of Chiral Metal Nanoparticle Assemblies. *Nano Lett.* **2010**, *10*, 2580–2587.

[70] Shen, X.; Song, C.; Wang, J.; Shi, D.; Wang, Z.; Liu, N.; Ding, B. Rolling Up Gold Nanoparticle-Dressed DNA Origami into Three-Dimensional Plasmonic Chiral Nanostructures. *J. Am. Chem. Soc.* **2012**, *134*, 146–149.

[71] Song, C.; Blaber, M. G.; Zhao, G.; Zhang, P.; Fry, H. C.; Schatz, G. C.; Rosi, N. L. Tailorable Plasmonic Circular Dichroism Properties of Helical Nanoparticle Superstructures. *Nano Lett.* **2013**, *13*, 3256–3261.

[72] Schäferling, M.; Dregely, D.; Hentschel, M.; Giessen, H. Tailoring Enhanced Optical Chirality: Design Principles for Chiral Plasmonic Nanostructures. *Phys. Rev. X* **2012**, *2*, 031010.

[73] Guerrero-Martínez, A.; Auguié, B.; Alonso-Gómez, J. L.; Džolić, Z.; Gómez-Graña, S.; Žinić, M.; Cid, M. M.; Liz-Marzán, L. M. Intense Optical Activity from Three-Dimensional Chiral Ordering of Plasmonic Nanoantennas. *Angew. Chemie Int. Ed.* **2011**, *50*, 5499–5503.

[74] Fan, Z.; Govorov, A. O. Chiral Nanocrystals: Plasmonic Spectra and Circular Dichroism. *Nano Lett.* **2012**, *12*, 3283–3289.

[75] Shemer, G.; Krichevski, O.; Markovich, G.; Molotsky, T.; Lubitz, I.; Kotlyar, A. B. Chirality of Silver Nanoparticles Synthesized on DNA. *J. Am. Chem. Soc.* **2006**, *128*, 11006–11007.

[76] Ren, M.; Plum, E.; Xu, J.; Zheludev, N. I. Giant Nonlinear Optical Activity in a Plasmonic Metamaterial. *Nat. Commun.* **2012**, *3*, 833.

[77] Hentschel, M.; Schäferling, M.; Weiss, T.; Liu, N.; Giessen, H. Three-Dimensional Chiral Plasmonic Oligomers. *Nano Lett.* **2012**, *12*, 2542–2547.

[78] Shen, X.; Asenjo-Garcia, A.; Liu, Q.; Jiang, Q.; García de Abajo, F. J.; Liu, N.; Ding, B. Three-Dimensional Plasmonic Chiral Tetramers Assembled by DNA Origami. *Nano Lett.* **2013**, *13*, 2128–2133.

[79] Yan, W.; Xu, L.; Xu, C.; Ma, W.; Kuang, H.; Wang, L.; Kotov, N. A. Self-Assembly of Chiral Nanoparticle Pyramids with Strong R / S Optical Activity. *J. Am. Chem. Soc.* **2012**, *134*, 15114–15121.

[80] Chen, W.; Bian, A.; Agarwal, A.; Liu, L.; Shen, H.; Wang, L.; Xu, C.; Kotov, N. A. Nanoparticle Superstructures Made by Polymerase Chain Reaction: Collective Interactions of Nanoparticles and a New Principle for Chiral Materials. *Nano Lett.* **2009**, *9*, 2153–2159.

[81] Belardini, A.; Larciprete, M. C.; Centini, M.; Fazio, E.; Sibilia, C.; Chiappe, D.; Martella, C.; Toma, A.; Giordano, M.; Buatier de Mongeot, F. Circular Dichroism in the Optical Second-Harmonic Emission of Curved Gold Metal Nanowires. *Phys. Rev. Lett.* **2011**, *107*, 257401.

[82] Hu, L.; Huang, Y.; Fang, L.; Chen, G.; Wei, H.; Fang, Y. Fano Resonance Assisting Plasmonic Circular Dichroism from Nanorice Heterodimers for Extrinsic Chirality. *Sci. Rep.* **2015**, *5*, 16069.

[83] De Leon, I.; Horton, M. J.; Schulz, S. A.; Upham, J.; Banzer, P.; Boyd, R. W. Strong, Spectrally-Tunable Chirality in Diffractive Metasurfaces. *Sci. Rep.* **2015**, *5*, 13034.

[84] Yokoyama, A.; Yoshida, M.; Ishii, A.; Kato, Y. K. Giant Circular Dichroism in Individual Carbon Nanotubes Induced by Extrinsic Chirality. *Phys. Rev. X* **2014**, *4*, 011005.

[85] Lu, X.; Wu, J.; Zhu, Q.; Zhao, J.; Wang, Q.; Zhan, L.; Ni, W. Circular Dichroism from Single Plasmonic Nanostructures with Extrinsic Chirality. *Nanoscale* **2014**, *6*, 14244–14253.

[86] Cao, T.; Wei, C.; Mao, L.; Li, Y. Extrinsic 2D Chirality: Giant Circular Conversion Dichroism from a Metal-Dielectric-Metal Square Array. *Sci. Rep.* **2014**, *4*, 7442.

[87] Plum, E.; Liu, X.-X.; Fedotov, V. A.; Chen, Y.; Tsai, D. P.; Zheludev, N. I. Metamaterials: Optical Activity without Chirality. *Phys. Rev. Lett.* **2009**, *102*, 113902.

[88] Maoz, B. M.; Ben Moshe, A.; Vestler, D.; Bar-Elli, O.; Markovich, G. Chiroptical Effects in Planar Achiral Plasmonic Oriented Nanohole Arrays. *Nano Lett.* **2012**, *12*, 2357–2361.

[89] Verbiest, T.; Kauranen, M.; Van Rompaey, Y.; Persoons, A. Optical Activity of Anisotropic Achiral Surfaces. *Phys. Rev. Lett.* **1996**, *77*, 1456–1459.

[90] Tang, Y.; Cohen, A. E. Enhanced Enantioselectivity in Excitation of Chiral Molecules by Superchiral Light. *Science (80-.).* **2011**, *332*, 333–336.

[91] Maoz, B. M.; Chaikin, Y.; Tesler, A. B.; Bar Elli, O.; Fan, Z.; Govorov, A. O.; Markovich, G. Amplification of Chiroptical Activity of Chiral Biomolecules by Surface Plasmons. *Nano Lett.* **2013**, *13*, 1203–1209.

[92] Gorodetski, Y.; Drezet, A.; Genet, C.; Ebbesen, T. W. Generating Far-Field Orbital Angular Momenta from Near-Field Optical Chirality. *Phys. Rev. Lett.* **2013**, *110*, 203906.

[93] Abdulrahman, N. A.; Fan, Z.; Tonooka, T.; Kelly, S. M.; Gadegaard, N.; Hendry, E.; Govorov, A. O.; Kadodwala, M. Induced Chirality through Electromagnetic Coupling between Chiral Molecular Layers and Plasmonic Nanostructures. *Nano Lett.* **2012**, *12*, 977–983.

[94] Govorov, A. O. Plasmon-Induced Circular Dichroism of a Chiral Molecule in the Vicinity of Metal Nanocrystals. Application to Various Geometries. *J. Phys. Chem. C* **2011**, *115*, 7914–7923.

[95] Slocik, J. M.; Govorov, A. O.; Naik, R. R. Plasmonic Circular Dichroism of Peptide-Functionalized Gold Nanoparticles. *Nano Lett.* **2011**, *11*, 701–705.

[96] Govorov, A. O.; Fan, Z.; Hernandez, P.; Slocik, J. M.; Naik, R. R. Theory of Circular Dichroism of Nanomaterials Comprising Chiral Molecules and Nanocrystals: Plasmon Enhancement, Dipole Interactions, and Dielectric Effects. *Nano Lett.* **2010**, *10*, 1374–1382.

[97] Lipkin, D. M. Existence of a New Conservation Law in Electromagnetic Theory. *J. Math. Phys.* **1964**, *5*, 696.

[98] Lebedev, P. N. Experimental Examination of Light Pressure. *Ann. Phys.* **1901**, *6*, 433.

[99] Nichols, E. F.; Hull, G. F. A Preliminary Communication on the Pressure of Heat and Light Radiation. *Phys. Rev. (Series I)* **1901**, *13*, 307–320.

[100] Ashkin, A. Acceleration and Trapping of Particles by Radiation Pressure. *Phys. Rev. Lett.* **1970**, *24*, 156–159.

[101] Ashkin, A.; Dziedzic, J. M. Optical Levitation by Radiation Pressure. *Appl. Phys. Lett.* **1971**, *19*, 283.

[102] Jonáš, A.; Zemánek, P. Light at Work: The Use of Optical Forces for Particle Manipulation, Sorting, and Analysis. *Electrophoresis* **2008**, *29*, 4813–4851.

[103] Hansen, P. M.; Bhatia, V. K.; Harrit, N.; Oddershede, L. Expanding the Optical Trapping Range of Gold Nanoparticles. *Nano Lett.* **2005**, *5*, 1937–1942.

[104] Zemánek, P.; Jonáš, A.; Šrámek, L.; Liška, M. Optical Trapping of Nanoparticles and Microparticles by a Gaussian Standing Wave. *Opt. Lett.* **1999**, *24*, 1448.

[105] Saija, R.; Denti, P.; Borghese, F.; Maragò, O. M.; Iatì, M. A. Optical Trapping Calculations for Metal Nanoparticles Comparison with Experimental Data for Au and Ag Spheres. *Opt. Express* **2009**, *17*, 10231.

[106] Urban, A. S.; Carretero-Palacios, S.; Lutich, A. A.; Lohmüller, T.; Feldmann, J.; Jäckel, F. Optical Trapping and Manipulation of Plasmonic Nanoparticles: Fundamentals, Applications, and Perspectives. *Nanoscale* **2014**, *6*, 4458.

[107] Zelenina, A. S.; Quidant, R.; Nieto-Vesperinas, M. Enhanced Optical Forces between Coupled Resonant Metal Nanoparticles. *Opt. Lett.* **2007**, *32*, 1156.

[108] Xu, H.; Käll, M. Surface-Plasmon-Enhanced Optical Forces in Silver Nanoaggregates. *Phys. Rev. Lett.* **2002**, *89*, 246802.

[109] Prikulis, J.; Svedberg, F.; Käll, M.; Enger, J.; Ramser, K.; Goksör, M.; Hanstorp, D. Optical Spectroscopy of Single Trapped Metal Nanoparticles in Solution. *Nano Lett.* **2004**, *4*, 115–118.

[110] Bosanac, L.; Aabo, T.; Bendix, P. M.; Oddershede, L. B. Efficient Optical Trapping and Visualization of Silver Nanoparticles. *Nano Lett.* **2008**, *8*, 1486–1491.

[111] Pang, Y.; Gordon, R. Optical Trapping of a Single Protein. *Nano Lett.* **2012**, *12*, 402–406.

[112] Brzobohatý, O.; Šiler, M.; Trojek, J.; Chvátal, L.; Karásek, V.; Paták, A.; Pokorná, Z.; Mika, F.; Zemánek, P. Three-Dimensional Optical Trapping of a Plasmonic Nanoparticle Using Low Numerical Aperture Optical Tweezers. *Sci. Rep.* **2015**, *5*, 8106.

[113] Pelton, M.; Liu, M.; Kim, H. Y.; Smith, G.; Guyot-Sionnest, P.; Scherer, N. F. Optical Trapping and Alignment of Single Gold Nanorods by Using Plasmon Resonances. *Opt. Lett.* **2006**, *31*, 2075.

[114] Selhuber-Unkel, C.; Zins, I.; Schubert, O.; Sönnichsen, C.; Oddershede, L. B. Quantitative Optical Trapping of Single Gold Nanorods. *Nano Lett.* **2008**, *8*, 2998–3003.

[115] Toussaint, K. C.; Liu, M.; Pelton, M.; Pesic, J.; Guffey, M. J.; Guyot-Sionnest, P.; Scherer, N. F. Plasmon Resonance-Based Optical Trapping of Single and Multiple Au Nanoparticles. *Opt. Express* **2007**, *15*, 12017.

[116] Tong, L.; Righini, M.; Gonzalez, M. U.; Quidant, R.; Käll, M. Optical Aggregation of Metal Nanoparticles in a Microfluidic Channel for Surface-Enhanced Raman Scattering Analysis. *Lab Chip* **2009**, *9*, 193–195.

[117] Huang, L.; Maerkl, S. J.; Martin, O. J. Integration of Plasmonic Trapping in a Microfluidic Environment. *Opt. Express* **2009**, *17*, 6018.

[118] Guffey, M. J.; Scherer, N. F. All-Optical Patterning of Au Nanoparticles on Surfaces Using Optical Traps. *Nano Lett.* **2010**, *10*, 4302–4308.

[119] Quidant, R.; Girard, C. Surface-Plasmon-Based Optical Manipulation. *Laser Photonics Rev.* **2008**, *2*, 47–57.

[120] Righini, M.; Volpe, G.; Girard, C.; Petrov, D.; Quidant, R. Surface Plasmon Optical Tweezers: Tunable Optical Manipulation in the Femtonewton Range. *Phys. Rev. Lett.* **2008**, *100*, 186804.

[121] Roxworthy, B. J.; Ko, K. D.; Kumar, A.; Fung, K. H.; Chow, E. K. C.; Liu, G. L.; Fang, N. X.; Toussaint, K. C. Application of Plasmonic Bowtie Nanoantenna Arrays for Optical Trapping, Stacking, and Sorting. *Nano Lett.* **2012**, *12*, 796–801.

[122] Righini, M.; Zelenina, A. S.; Girard, C.; Quidant, R. Parallel and Selective Trapping in a Patterned Plasmonic Landscape. *Nat. Phys.* **2007**, *3*, 477–480.

[123] Pang, Y.; Gordon, R. Optical Trapping of 12 Nm Dielectric Spheres Using Double-Nanoholes in a Gold Film. *Nano Lett.* **2011**, *11*, 3763–3767.

[124] Zhang, W.; Huang, L.; Santschi, C.; Martin, O. J. F. Trapping and Sensing 10 Nm Metal Nanoparticles Using Plasmonic Dipole Antennas. *Nano Lett.* **2010**, *10*, 1006–1011.

[125] Huang, J.-S.; Yang, Y.-T. Origin and Future of Plasmonic Optical Tweezers. *Nanomaterials* **2015**, *5*, 1048–1065.

[126] Chen, C.; Juan, M. L.; Li, Y.; Maes, G.; Borghs, G.; Van Dorpe, P.; Quidant, R. Enhanced Optical Trapping and Arrangement of Nano-Objects in a Plasmonic Nanocavity. *Nano Lett.* **2012**, *12*, 125–132.

[127] Wang, K.; Schonbrun, E.; Steinvurzel, P.; Crozier, K. B. Trapping and Rotating Nanoparticles Using a Plasmonic Nano-Tweezer with an Integrated Heat Sink. *Nat. Commun.* **2011**, *2*, 469.

[128] Grigorenko, A. N.; Roberts, N. W.; Dickinson, M. R.; Zhang, Y. Nanometric Optical Tweezers Based on Nanostructured Substrates. *Nat. Photonics* **2008**, *2*, 365–370.

[129] Volpe, G.; Quidant, R.; Badenes, G.; Petrov, D. Surface Plasmon Radiation Forces. *Phys. Rev. Lett.* **2006**, *96*, 238101.

[130] Shao, L.; Yang, Z.-J.; Andrén, D.; Johansson, P.; Käll, M. Gold Nanorod Rotary Motors Driven by Resonant Light Scattering. *ACS Nano* **2015**, *9*, 12542–12551.

[131] Ebbens, S. J.; Howse, J. R. In Pursuit of Propulsion at the Nanoscale. *Soft Matter* **2010**, *6*, 726.

[132] Chang, S. T.; Paunov, V. N.; Petsev, D. N.; Velev, O. D. Remotely Powered Self-Propelling Particles and Micropumps Based on Miniature Diodes. *Nat. Mater.* **2007**, *6*, 235–240.

[133] Draine, B. T. The Discrete-Dipole Approximation and Its Application to Interstellar Graphite Grains. *Astrophys. J.* **1988**, *333*, 848.

[134] Gordon, J. P. Radiation Forces and Momenta in Dielectric Media. *Phys. Rev. A* **1973**, *8*, 14.

[135] Albaladejo, S.; Marqués, M. I.; Laroche, M.; Sáenz, J. J. Scattering Forces from the Curl of the Spin Angular Momentum of a Light Field. *Phys. Rev. Lett.* **2009**, *102*, 113602.

[136] Chaumet, P. C.; Billaudeau, C. Coupled Dipole Method to Compute Optical Torque: Application to a Micropropeller. *J. Appl. Phys.* **2007**, *101*, 023106.

[137] Marston, P. L.; Crichton, J. H. Radiation Torque on a Sphere Caused by Circularly-Polarized Electromagnetic Wave. *Phys. Rev. A* **1984**, *30*, 2508–2516.

[138] Landau, L. D.; Lifshitz, E. M. *Fluid Mechanics (1st ed.)*; Pergamon Pres Ltd., Oxford, 1959.

[139] Kong, D.; Lin, W.; Pan, Y.; Zhang, K. Swimming Motion of Rod-Shaped Magnetotactic Bacteria: The Effects of Shape and Growing Magnetic Moment. *Front. Microbiol.* **2014**, *5*, 1–11.

[140] Lacava, J.; Ouali, A.-A.; Raillard, B.; Kraus, T. On the Behaviour of Nanoparticles in Oil-in-Water Emulsions with Different Surfactants. *Soft Matter* **2014**, *10*, 1696.

[141] Saha, A.; John, V. T.; Bose, A. In Situ Assembly of Hydrophilic and Hydrophobic Nanoparticles at Oil–Water Interfaces as a Versatile Strategy To Form Stable Emulsions. *ACS Appl. Mater. Interfaces* **2015**, *7*, 21010–21014.

[142] Madivala, B.; Fransaer, J.; Vermant, J. Self-Assembly and Rheology of Ellipsoidal Particles at Interfaces. *Langmuir* **2009**, *25*, 2718–2728.

[143] Vogel, N.; Ally, J.; Bley, K.; Kappl, M.; Landfester, K.; Weiss, C. K. Direct Visualization of the Interfacial Position of Colloidal Particles and Their Assemblies. *Nanoscale* **2014**, *6*, 6879.

[144] Gibaud, T.; Barry, E.; Zakhary, M. J.; Henglin, M.; Ward, A.; Yang, Y.; Berciu, C.; Oldenbourg, R.; Hagan, M. F.; Nicastro, D.; *et al.* Reconfigurable Self-Assembly through Chiral Control of Interfacial Tension. *Nature* **2012**, *481*, 348–351.

[145] Paunov, V. N. Novel Method for Determining the Three-Phase Contact Angle of Colloid Particles Adsorbed at Air–Water and Oil–Water Interfaces. *Langmuir* **2003**, *19*, 7970–7976.

[146] Jing, D.; Bhushan, B. The Coupling of Surface Charge and Boundary Slip at the Solid–liquid Interface and Their Combined Effect on Fluid Drag: A Review. *J. Colloid Interface Sci.* **2015**, *454*, 152–179.

[147] Kelleher, C. P.; Wang, A.; Guerrero-García, G. I.; Hollingsworth, A. D.; Guerra, R. E.; Krishnatreya, B. J.; Grier, D. G.; Manoharan, V. N.; Chaikin, P. M. Charged Hydrophobic Colloids at an Oil-Aqueous Phase Interface. *Phys. Rev. E - Stat. Nonlinear, Soft Matter Phys.* **2015**, *92*, 062306.

[148] Park, B. J.; Lee, D. Dynamically Tuning Particle Interactions and Assemblies at Soft Interfaces: Reversible Order-Disorder Transitions in 2D Particle Monolayers. *Small* **2015**, *11*, 4560–4567.

[149] Dunér, G.; Garoff, S.; Przybycien, T. M.; Tilton, R. D. Transient Marangoni Transport of Colloidal Particles at the Liquid/liquid Interface Caused by Surfactant Convective-Diffusion under Radial Flow. *J. Colloid Interface Sci.* **2016**, *462*, 75–87.

[150] Dani, A.; Keiser, G.; Yeganeh, M.; Maldarelli, C. Hydrodynamics of Particles at an Oil–Water Interface. *Langmuir* **2015**, *31*, 13290–13302.

[151] Park, B. J.; Lee, M.; Lee, B.; Furst, E. M. Lateral Capillary Interactions between Colloids beneath an Oil–water Interface That Are Driven by out-of-Plane Electrostatic Double-Layer Interactions. *Soft Matter* **2015**, *11*, 8701–8706.

[152] Nikolaides, M. G.; Bausch, A. R.; Hsu, M. F.; Dinsmore, A. D.; Brenner, M. P.; Gay, C.; Weitz, D. A. Electric-Field-Induced Capillary Attraction between like-Charged Particles at Liquid Interfaces. *Nature* **2002**, *420*, 299–301.

[153] Jones, M. R.; Osberg, K. D.; Macfarlane, R. J.; Langille, M. R.; Mirkin, C. A. Templated Techniques for the Synthesis and Assembly of Plasmonic Nanostructures. *Chem. Rev.* **2011**, *111*, 3736–3827.

[154] Zhang, J.; Li, Y.; Zhang, X.; Yang, B. Colloidal Self-Assembly Meets Nanofabrication: From Two-Dimensional Colloidal Crystals to Nanostructure Arrays. *Adv. Mater.* **2010**, *22*, 4249–4269.

[155] Ogaki, R.; Cole, M. A.; Sutherland, D. S.; Kingshott, P. Microcup Arrays Featuring Multiple Chemical Regions Patterned with Nanoscale Precision. *Adv. Mater.* **2011**, *23*, 1876–1881.

[156] Masson, J.-F.; Murray-Méthot, M.-P.; Live, L. S. Nanohole Arrays in Chemical Analysis: Manufacturing Methods and Applications. *Analyst* **2010**, *135*, 1483.

[157] Dahlin, A. B.; Mapar, M.; Xiong, K.; Mazzotta, F.; Höök, F.; Sannomiya, T. Plasmonic Nanopores in Metal-Insulator-Metal Films. *Adv. Opt. Mater.* **2014**, *2*, 556–564.

[158] Langhammer, C.; Schwind, M.; Kasemo, B.; Zorić, I. Localized Surface Plasmon Resonances in Aluminum Nanodisks. *Nano Lett.* **2008**, *8*, 1461–1471.

[159] Svedendahl, M.; Johansson, P.; Käll, M. Complete Light Annihilation in an Ultrathin Layer of Gold Nanoparticles. *Nano Lett.* **2013**, *13*, 3053–3058.

[160] Chen, S.; Svedendahl, M.; Käll, M.; Gunnarsson, L.; Dmitriev, A. Ultrahigh Sensitivity Made Simple: Nanoplasmonic Label-Free Biosensing with an Extremely Low Limit-of-Detection for Bacterial and Cancer Diagnostics. *Nanotechnology* **2009**, *20*, 434015.

[161] Shegai, T.; Chen, S.; Miljković, V. D.; Zengin, G.; Johansson, P.; Käll, M. A Bimetallic Nanoantenna for Directional Colour Routing. *Nat. Commun.* **2011**, *2*, 481.

[162] Pakizeh, T.; Dmitriev, A.; Abrishamian, M. S.; Granpayeh, N.; Käll, M. Structural Asymmetry and Induced Optical Magnetism in Plasmonic Nanosandwiches. *J. Opt. Soc. Am. B* **2008**, *25*, 659.

[163] Wadell, C.; Antosiewicz, T. J.; Langhammer, C. Optical Absorption Engineering in Stacked Plasmonic Au–SiO 2 –Pd Nanoantennas. *Nano Lett.* **2012**, *12*, 4784–4790.

[164] Syrenova, S.; Wadell, C.; Langhammer, C. Shrinking-Hole Colloidal Lithography: Self-Aligned Nanofabrication of Complex Plasmonic Nanoantennas. *Nano Lett.* **2014**, *14*, 2655–2663.

[165] Hentschel, M.; Dregely, D.; Vogelgesang, R.; Giessen, H.; Liu, N. Plasmonic Oligomers: The Role of Individual Particles in Collective Behavior. *ACS Nano* **2011**, *5*, 2042–2050.

[166] Verre, R.; Svedendahl, M.; Länk, N. O.; Yang, Z. J.; Zengin, G.; Antosiewicz, T. J.; Käll, M. Directional Light Extinction and Emission in a Metasurface of Tilted Plasmonic Nanopillars. *Nano Lett.* **2016**, *16*, 98–104.

[167] Cai, Y.; Li, Y.; Nordlander, P.; Cremer, P. S. Fabrication of Elliptical Nanorings with Highly Tunable and Multiple Plasmonic Resonances. *Nano Lett.* **2012**, *12*, 4881–4888.

[168] Bochenkov, V. E.; Sutherland, D. S. From Rings to Crescents: A Novel Fabrication Technique Uncovers the Transition Details. *Nano Lett.* **2013**, *13*, 1216–1220.

[169] Warmack, R. J.; Humphrey, S. L. Observation of Two Surface-Plasmon Modes on Gold Particles. *Phys. Rev. B* **1986**, *34*, 2246–2252.

[170] Siegfried, T.; Ekinci, Y.; Martin, O. J. F.; Sigg, H. Engineering Metal Adhesion Layers That Do Not Deteriorate Plasmon Resonances. *ACS Nano* **2013**, *7*, 2751–2757.

[171] Frank, B.; Yin, X.; Schäferling, M.; Zhao, J.; Hein, S. M.; Braun, P. V; Giessen, H. Large-Area 3D Chiral Plasmonic Structures. *ACS Nano* **2013**, *7*, 6321–6329.

[172] Yu, N.; Capasso, F. Flat Optics with Designer Metasurfaces. *Nat. Mater.* **2014**, *13*, 139–150.

[173] Karimi, E.; Schulz, S. A.; De Leon, I.; Qassim, H.; Upham, J.; Boyd, R. W. Generating Optical Orbital Angular Momentum at Visible Wavelengths Using a Plasmonic Metasurface. *Light Sci. Appl.* **2014**, *3*, e167.

[174] Pors, A.; Nielsen, M. G.; Eriksen, R. L.; Bozhevolnyi, S. I. Broadband Focusing Flat Mirrors Based on Plasmonic Gradient Metasurfaces. *Nano Lett.* **2013**, *13*, 829–834.

[175] Tsai, W.-Y.; Huang, J.-S.; Huang, C.-B. Selective Trapping or Rotation of Isotropic Dielectric Microparticles by Optical Near Field in a Plasmonic Archimedes Spiral. *Nano Lett.* **2014**, *14*, 547–552.